Phase-field study of IMC growth in Sn–Cu/Cu solder joints including elastoplastic effects

A. Durga[a,b], P. Wollants[a], N. Moelans[a,1]

[a] *Department of Materials Engineering, Faculty of Engineering, KU Leuven, Kasteelpark Arenberg 44 Bus 2450, BE-3001 Leuven, Belgium*
[b] *Department of Materials Science and Engineering, KTH Royal Institute of Technology, Brinellvägen 23, S-10044 Stockholm, Sweden*

Abstract

In this article, we aim to study the problem of the growth of intermetallic phases in solder joints undergoing mechanical deformation, using a phase-field model for multi-phase systems that can treat diffusion, elastic and plastic deformation. A suitable model is formulated and applied to Sn–Cu/Cu lead-free solder joints. The growth of the intermetallic layers during solid-state annealing is simulated for different strain states. We assess the values of stiffness tensors available in literature and perform *ab initio* calculations to support the selection of reasonable values from literature. We also perform a parametric study with different eigenstrain values and applied strains. We find that there is a significant effect of the considered eigenstrains and applied strains on the growth kinetics of the system and parabolic growth kinetics is followed in cases where the intermetallic layers grow. We thereby establish the importance of strain in the growth of intermetallic layers and the need for more targeted experiments on the role of strain in the reliability of the solder joint.

Keywords: Phase-field modelling, Lead-free solders, Microstructure, Deformation, *ab initio* calculations

1. Introduction

Lead-free soldering has been an active area of research for the last decade following the ban on the usage of lead in microelectronic devices. Sn-Cu based lead-free solder alloys

Email addresses: durga87@gmail.com, durgaa@kth.se (A. Durga), patrick.wollants@kuleuven.be (P. Wollants), nele.moelans@kuleuven.be (N. Moelans)
[1] Corresponding author

are mostly used in electronic packaging and high temperature applications [1, 2]. During the soldering process, Cu_3Sn and Cu_6Sn_5 intermetallic compound (IMC) layers form at the interface between the Cu substrate and the Sn-Cu solder alloy. When the layers are thin, the intermetallic phases give strength to the solder joint. However, due to the large difference in mechanical properties between the hard, but brittle, IMCs and the soft Cu-substrate and Sn-Cu solder, regions vulnerable to crack formation are created [3] when the IMC layers grow in thickness. Therefore, controlling the growth of the IMCs is key to improving the reliability of the solder joints, however, is till today not achieved, despite huge experimental efforts [4, 5, 6, 7]. Due to the large number of influencing factors, there is often a large discrepancy between experimental findings from different studies.

Some experimental studies indicate that, besides annealing temperature and duration, mechanical stresses or deformation, experienced by the solder joint during processing or in service conditions, may affect the growth kinetics of the IMCs. Lin et. al [8] have, for example, reported that an applied tensile or compressive strain of 2.5% increases the growth rate of the Cu_6Sn_5 layer, while that of the Cu_3Sn is retarded for compressive strain, when annealing at 200 °C. Based on their experimental observations, it was concluded that the enhanced growth of Cu_6Sn_5 for compressive stress may be devoted to the smaller grain size for Cu_6Sn_5 when compressive stress was applied, which resulted in an increase of the diffusion through the Cu_6Sn_5 layer. A similar effect was observed in other lead-free solder joints also, for example, in Sn-Ag/Cu joint [9]. In another study, Lin *et al.* [10] have found that an applied strain of 0.34% did not affect the growth rate of the IMCs although the morphology was influenced by it. Panchenko [11] has observed that the Cu_3Sn thickness increased with increased bonding pressure (of upto 2.42 MPa) during the processing of a SnAg/Cu interconnect at 250 °C. Unfortunately, the experimental observations only do not give sufficient information to fully understand the way mechanical stresses or strains may affect the growth behavior of IMCs in solder joints.

Phase-field simulations of IMC growth in lead-free solder joints have been reported in literature, including diffusion [12, 13, 14] and mechanical deformation [15, 16, 17]. Xiong and Huang [15] have used a phase-field model taking into account only elastic effects (and electromigration) in order to simulate the IMC growth in a Cu/Sn-microbump/Cu structure.

They predicted that at 150 °C, Cu_3Sn grains grow at a higher rate under external compressive stress while Cu_6Sn_5 grows faster under external tensile stress. They have implemented a phase-field model with a Vegard's law type formulation of eigenstrain and they consider only elastic deformation even though high stresses above the yield limit are reached. It is thus clear that plastic effects must be considered in the phase-field model to obtain realistic results. Hektor et al. [17] were the first to perform diffusion-deformation coupled multi-phase simulations of Cu_6Sn_5 growth at Sn/Cu joint at room temperature ageing, including effects of plastic deformation, giving a much more realistic representation than all the models before. However, they have interpolated the elastic energy density in the phase-field model using a Reuss-Sachs' condition, which was shown [18] to lead to interface-width-dependent excess energy at the interface, which is not physically present. Since in phase-field simulations, the width of the interfaces is usually enlarged artificially to limit the computational requirements, the effect of this excess energy can become excessively high [18], depending on the size of the grains, the width of the diffuse interface assumed in the phase-field model and the heterogeneity in elastic properties between the different phases. Moreover, they did not include the Cu_3Sn phase in their simulations, while experiments show that this phase is present during annealing and one can expect that its growth will affect the stress conditions in the joint and the growth of the Cu_6Sn_5 phase. Since they observe linear growth kinetics of the IMC layers, we believe that their simulations only consider initial transient growth and did not reach the steady-state regime where parabolic growth kinetics are expected generally for intermetallic growth even when mechanical effects are present [19, 20]. Moreover, only the effect of eigenstrains caused by the volume change associated with the growth of the IMC, in the absence of applied strain, is considered.

In general, multi-phase phase-field models coupling composition evolution and elasto-plastic deformation have recently been developed by a few groups. Capturing the macroscopic effect of the presence and movement of dislocations through phenomenological plasticity-related variables, phase-field models have been developed and implemented by [21, 22, 23, 24, 25, 26, 27, 28]. A generic method to include hardening in the plastic regime was proposed by Gaubert *et al.* [23], into which a crystal plasticity framework was later incorporated [21]. Cottura *et al.* [24] applied this model to study rafting in Ni-based superalloys.

Cottura *et al.* [29] further developed this study by coupling the phase-field model to strain-gradient crystal plasticity through dislocation densities. The authors developed [18, 30] a quantitative phase-field model coupling chemical and elastic strain energies, satisfying local both chemical and mechanical equilibrium at the interface. We validated the model in 2D and 3D for cases of inhomogeneous anisotropic elastic moduli and applied strains. In a series of papers, Schneider and co-workers developed [31] a quantitative phase-field model for including elastic energy, which was validated for the condition of applied stress, which they further developed to couple with chemical composition evolution [32] and extended to a multi-phase elasto-plastic coupled formulation [27].

The purpose of this study is to simulate the effect of different strain states on the IMC growth kinetics in Cu/Cu-Sn solder joints including both elastic and plastic deformation, to understand better the role and effect of various mechanical loading conditions. Therefore, we first introduce a multi-phase phase-field model satisfying local interfacial equilibrium while treating diffusion [33, 34] and coupled with the scheme we introduced [18, 30] for including elastic energy quantitatively and the plasticity formulation developed by Gaubert *et al.* [23]. Secondly, various simulations will be performed with this model. Different from the study of Hektor *et al.* [17], in this work, the simultaneous growth of Cu_3Sn and Cu_6Sn_5 layers will be considered and sufficiently long annealing times will be taken to verify whether a steady-state regime with parabolic growth kinetics can be obtained in the presence of strains. Moreover, besides the effect of eigenstrains due to the formation of the IMC layers, the effect of applied tensile and compressive strain on top of them will be studied. Since the work of Hektor *et al.* [17] shows that the initially scalloped morphology of the Cu_6Sn_5 layer evolves towards a morphology with almost flat interfaces during annealing, structures with flat interfaces will be considered in this study to reduce the computation time, thereby enabling quantitative analysis of the long-term annealing behavior. Finally, as part of this work, we have performed *ab initio* calculations of the stiffnesses of the pure Cu, Cu_3Sn, and pure Sn phases, in addition to the data available in literature and in order to support the selection of a reasonable value among the several, but scattered, values reported in the literature.

The rest of this paper is organised as follows. The phase-field model for multiphase systems combining diffusion, elastic and plastic deformation is formulated in Section 2. The

input data from experiments and theoretical estimates that have been used in the simulations are discussed in Section 3. Simulations of $Cu/Cu_3Sn/Cu_6Sn_5/Sn$ layers representing annealing of Sn-Cu/Cu lead-free solder joints at 180 °C are performed for different deformation conditions (Section 4).

2. Phase-field model formulation

In a phase-field model, the microstructure is represented by phase-field variables which vary smoothly across different domains, giving rise to diffuse interfaces. At the mesoscale, the interface regions are usually taken much wider than the physically observed values in order to minimise computational resources. This is possible if special care is given to the phase-field model formulation to ensure that the expected bulk and interfacial properties and local chemical and mechanical equilibrium at the interfaces are obtained, so that the results become independent of the choice of the diffuse interface width. In this work, we use the multi-phase phase-field framework developed by Moelans [34] and incorporate the quantitative elastic energy formulation introduced by the authors [18, 30] and plastic deformation by Gaubert *et al.* [23] and Cottura *et al.* [24]. The elastoplastic formulation was validated for two–phase systems with planar interfaces by the authors [35] (reproduced in Appendix D) using an analytical solution.

We consider a system with two chemical components and N phases ($\rho = \alpha,\beta,...$). It is assumed that the system is at a constant temperature. Only one grain per phase is considered. Undeformed α phase is taken as the reference state, therefore the eigenstrain in α is 0: $\epsilon_{ij}^{*,\alpha} = 0$.

The following phase-field variables, which are functions of space $\boldsymbol{r}$ and time t, are taken into account in order to simulate diffusion and mechanical deformation: c($\boldsymbol{r}$,t), the chemical composition, the order parameters η_ρ, representing the different phases ρ, which take the value 1 inside the bulk of ρ phase and transition to 0 at the boundaries with other phases:

$$\boldsymbol{\eta(r,t)} = \eta_\alpha(\boldsymbol{r},t), \eta_\beta(\boldsymbol{r},t), ..., \eta_\rho(\boldsymbol{r},t), ..., \eta_N(\boldsymbol{r},t),$$

and the elastic and plastic strain fields: $\epsilon_{ij}^{el}(\boldsymbol{r},t)$, $\epsilon_{ij}^{pl}(\boldsymbol{r},t)$.

In order to define bulk properties of the system (compositions, different types of energies, etc.) at the diffuse interface, the following interpolation function is used:

$$h_\alpha(\boldsymbol{\eta}) = \phi_\alpha(\boldsymbol{\eta}) = \frac{|\boldsymbol{\eta_\alpha}|^2}{\sum_{\rho=1}^{N} |\boldsymbol{\eta_\rho}|^2}, \tag{1}$$

for which $\sum_{\rho=1}^{N} \phi_\rho = 1$. ϕ_ρ can be interpreted as the phase fraction of phase ρ.

For this work, a total free energy functional with the following contributions is defined as:

$$F = \int_V \left[f^{ch}(\boldsymbol{\eta_\rho}, \boldsymbol{c}) + f^{int}(\boldsymbol{\eta_\rho}) + f^{el}(\boldsymbol{\eta_\rho}, \boldsymbol{\epsilon^{el}_{ij}}) + f^{vp}(\boldsymbol{\eta_\rho}, \boldsymbol{\epsilon^{pl}_{ij}}) \right] \mathrm{d}V, \tag{2}$$

where f^{ch} is the chemical free energy density, f^{int} the interfacial energy density, f^{el} the elastic strain energy density, and f^{vp} the plastic strain energy density. The formulation of f^{int}, f^{ch} and f^{el} are taken from our previous works and are discussed in Appendix A.

For this work, the viscoplastic strain energy density f^{vp} was added to these models, extending the viscoplastic energy formulation of Gaubert *et al.* [23] to multi-phase systems. Hardening is not considered in this study. For each phase, plastic strain $\epsilon^{pl,\rho}_{ij}$ and cumulative plastic strain $p^\rho = \int_t |\dot{\epsilon^{pl,\rho}_{ij}}| dt$ are introduced. The cumulative plastic strain rate evolution is given by [23]:

$$\dot{p^\rho} = \left\langle \frac{J_2(\sigma^\rho_{ij}) - R^\rho_0}{K^\rho} \right\rangle^n, \tag{3}$$

where R^ρ_0 is the yield stress, K^ρ is a scaling parameter, n the hardening exponent, and the von Mises stress $J_2(\sigma^\rho_{ij}) = \sqrt{3/2\ (\sigma^\rho_{ij})'(\sigma^\rho_{ij})'}$, with $'$ denoting the deviatoric part. $<>$ denotes the positive part of the enclosed term; therefore, this term is zero in the phases in which von Mises stress is less than the yield stress. For the multi-phase system, the viscoplastic strain energy density f^{vp} is then interpolated as

$$f^{vp} = \sum_{\rho=1}^{N} \phi_\rho f^{vp,\rho}. \tag{4}$$

where $f^{vp,\rho} = R^\rho_0 p^\rho$.

The evolution equation for the conserved variables is given by:

$$\frac{\partial c}{\partial t} = -\overrightarrow{\nabla}.\overrightarrow{J} = \overrightarrow{\nabla}.M(\boldsymbol{\eta}, \boldsymbol{c})\overrightarrow{\nabla}\frac{\delta F(\boldsymbol{\eta}, \boldsymbol{c}, \boldsymbol{\epsilon_{ij}^{el}}, \boldsymbol{\epsilon_{ij}^{pl}})}{\delta c} = \overrightarrow{\nabla}.\left[\left[\sum_{\rho=1}^{N}\phi_\rho M^\rho\right]\overrightarrow{\nabla}\frac{\partial f^{ch}}{\partial c}\right], \tag{5}$$

where M^ρ is the interdiffusion mobility of phase ρ. It is related to the interdiffusion coefficient $\tilde{D}^\rho$ as:

$$M^\rho = \frac{1}{V_m}\frac{\tilde{D}^\rho}{\frac{\partial^2 f^{ch,\rho}}{\partial (c^\rho)^2}}, \tag{6}$$

where V_m, the molar volume, is taken as a constant and the same for each phase and $f^{ch,\rho}$ is the composition-dependent chemical bulk free energy of phase ρ (introduced in Appendix A.1).

For non-conserved variables, a Ginzburg-Landau type equation is used:

$$\begin{aligned}\frac{\partial \eta_\rho}{\partial t} &= -L(\boldsymbol{\eta})\frac{\delta F(\boldsymbol{\eta}, \boldsymbol{r})}{\delta \eta_\rho} \\ &= -L(\boldsymbol{\eta})\left(\frac{\partial f^{ch}}{\partial \eta_\rho} + \frac{\partial f^{int}}{\partial \eta_\rho} + \frac{\partial f^{el}}{\partial \eta_\rho} + \frac{\partial f^{vp}}{\partial \eta_\rho}\right),\end{aligned} \tag{7}$$

where $L(\boldsymbol{\eta}) = \left(\sum_{\rho,\sigma} L_{\rho,\sigma}\eta_\rho\eta_\sigma\right) / \left(\sum_{\rho,\sigma}\eta_\rho\eta_\sigma\right)$, with $L_{\rho,\sigma}$ related to the interface mobility of ρ/σ interface. For diffusion-controlled growth,

$$L_{\rho,\sigma} = \frac{4m}{3\kappa(c_{eq}^\rho - c_{eq}^\sigma)^2}\frac{M^\rho + M^\sigma}{2}, \tag{8}$$

where c_{eq}^ρ and c_{eq}^σ are the equilibrium compositions of the phases ρ and σ respectively.

The plastic strain evolution for each phase is given by:

$$\frac{\partial \epsilon_{ij}^{pl,\rho}}{\partial t} = \frac{3}{2}\dot{p^\rho}\frac{\sigma_{ij}^\rho}{J_2(\sigma_{ij}^\rho)}. \tag{9}$$

3. Simulation details

3.1. Phase-field model implementation

In diffusion-controlled phase transformations, the chemical diffusion is much slower than the relaxation of displacements. Therefore, at each time step, the stresses and strains at mechanical equilibrium are calculated after solving the displacement field using the spectral

iterative perturbation method of Hu and Chen [36]. Initially, the plastic strains are assumed to be zero. These later take non-zero values in the phases that plastically deform. The driving forces for phase evolution from the chemical, interfacial, elastic and plastic contributions are calculated as formulated in [34], Appendix A.3, and Section 2. The evolution equations for the phase-field variables and the plastic strain are solved at every time step using finite difference discretisation in order to obtain the composition field and the microstructure represented by the order parameters.

3.2. System definition and initialisation of the phase-field simulations

Diffusion and mechanical deformation in Sn-Cu/Cu solder joints during solid-state annealing at 180 °C are simulated in this work. The phases ρ = Fcc-Cu, Cu_3Sn, Cu_6Sn_5, and Bct-Sn are considered (Figure 1). One-dimensional systems of 256 grid points (with 2 grid points in the y direction in order to use the spectral method for solving the displacement field) and with grid size Δx = 0.1 μm are considered. The width of the layers are taken as 10.8 μm of Cu, 2 μm of Cu_3Sn, 2 μm of Cu_6Sn_5, and 10.8 μm of Sn. The time step is taken as Δt = 0.01 s. For cases with eigenstrains based on volume change ('NoApp_VolEig', 'AppTensY_VolEig', 'AppCompY_VolEig', and 'AppCompX_VolEig', see section 3.9 and Table 1), Δx = 0.05 μm and system size of 4 $\times$ 512 grid points was used, since the diffuse interface width had to be taken narrower in these cases to assure stability of the η profiles.

The initial compositions of the phases are taken as $c_i^{Fcc-Cu} = 0.026$, $c_i^{Cu_3Sn} = 0.25$, $c_i^{Cu_6Sn_5} = 0.455$, and $c_i^{Bct-Sn} = 0.999958$, expressed as molar fraction of Sn. The compositions of Fcc-Cu and Bct-Sn correspond to their values at equilibrium with Cu_3Sn and Cu_6Sn_5 at 180 °C respectively.

3.3. Gibbs energies of the Cu–Sn system

The Cu–Sn system is part of the COST 531 thermodynamic database for lead-free solders [37] and also of the NIST database for solder alloys [38], providing us with a composition dependence of the Gibbs energies of these phases. However, the Cu_3Sn and Cu_6Sn_5 phases are treated as stoichiometric compounds in these databases, and hence cannot give rise to gradients in chemical potential needed to drive the diffusion in the phase-field simulations.

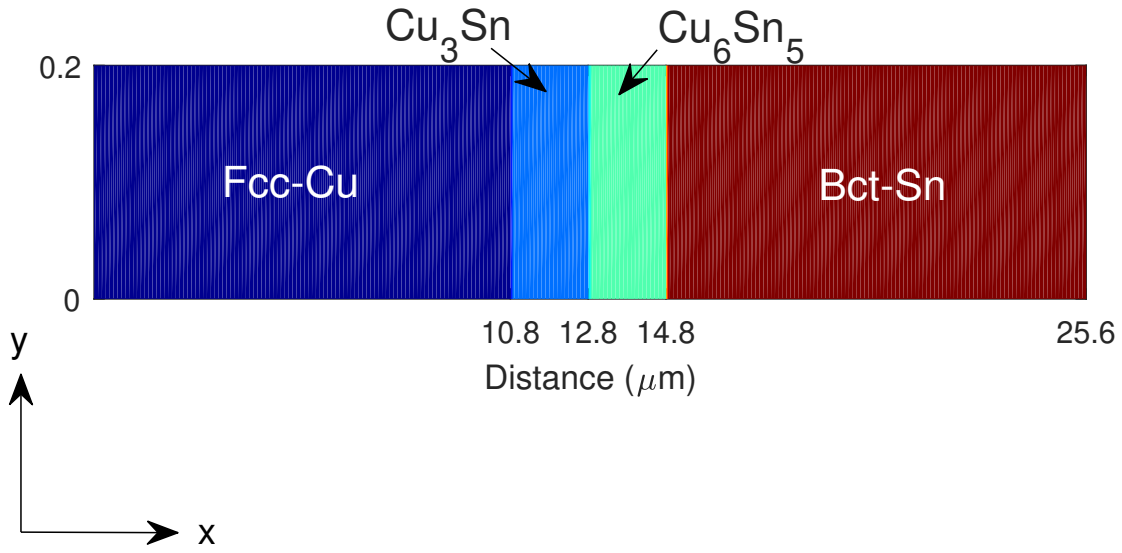

Figure 1: Initial structure (figure not to scale) of size 0.2 μm $\times$ 25.6μm used to simulate Cu/Sn-Cu solder joint under different conditions

Bct-Sn is treated as a stoichiometric compound in the COST 531 database. A composition-dependent Gibbs energy description is available in the NIST database, however, one with a miscibility gap, which gave complications in the phase-field simulations. Therefore, a parabolic composition dependence of the Gibbs energy for all phases, of the form

$$f^{ch,\rho} = \frac{A^\rho}{2}(c - c_0^\rho)^2 + B^\rho(c - c_0^\rho) + C^\rho, \tag{10}$$

was assumed. This avoids the difficulties associated with assessing sublattice models containing many parameters [39] for the stoichiometric phases and is computationally more efficient in the phase-field simulations. Moreover, in this case, since the compositions in the different phases are not expected to deviate much from equilibrium, a parabolic composition dependence with accurate fit near the equilibrium composition of each phase contains all the

required thermodynamic information. The fitting of the parabolic descriptions is done such that, for the solution phases, Fcc-Cu and Bct-Sn, the equilibrium composition and Gibbs energy, diffusion potential (i.e. first derivative of the Gibbs energy) and second derivative of the Gibbs energy at the equilibrium composition (as calculated using Thermo-Calc [40] with the COST 531 or NIST database at 180 °C) are reproduced in the simulations. The remaining model parameters were adapted, such that for the IMC phases, Cu_3Sn and Cu_6Sn_5, only a very narrow homogeneity range is obtained around the stoichiometric composition and such that the Gibbs energy (as calculated using Thermo-Calc with the COST 531 or NIST database at 180 °C) is reproduced in the simulations at the stoichiometric composition. The parameter values $A^\rho = 2.65 \cdot 10^{10}$, $1.794 \cdot 10^{11}$, $1.794 \cdot 10^{10}$, and $8.97 \cdot 10^{12}$ J/m^3 for, respectively, the Fcc-Cu, Cu_3Sn, Cu_6Sn_5, and Bct-Sn phase, $B^\rho = -4.09 \cdot 10^9$, $-4.09 \cdot 10^9$, $4.52 \cdot 10^8$, and $4.52 \cdot 10^8$ J/m^3, and $C^\rho = -1.71 \cdot 10^9$, $-2.61 \cdot 10^9$, $-2.66 \cdot 10^9$, and $-2.42 \cdot 10^9$ J/m^3 were obtained. The minima of the parabola are at compositions $c_0^\rho = 0.026$, 0.25, 0.455, and 0.999958 respectively, given as the molar fraction of Sn. Since the Cu-solubility in the Bct-Sn phase is extremely low (i.e. the equilibrium molar fraction of Sn, x_{Sn} is very close to 1), we had to take the A-values in the free energy density for the intermetallic phases smaller than the A^{Bct-Sn} obtained for the Bct-Sn phase to avoid that x_{Sn} in the Bct-Sn phase exceeds the value 1 at any moment in the simulations. A plot of the fitted parabolic functions are shown in Figure 2 along with the common tangents for the Fcc–Cu + Cu_3Sn, Cu_3Sn + Cu_6Sn_5 and Cu_6Sn_5 + Bct–Sn phase fields. The corresponding equilibrium compositions in terms of molar fraction of Sn calculated for these three regions are 0.0427 in Fcc-Cu + 0.2525 in Cu_3Sn, 0.2725 in Cu_3Sn + 0.4266 in Cu_6Sn_5, and 0.4544 in Cu_6Sn_5 + 1.0000 in Bct–Sn.

3.4. Eigenstrain

A full description of the eigenstrain in each phase, requires knowledge of the crystallographic structure of each phase and the orientation relationship between the different phases [41]. There are a few measurements of orientation relationships and lattice spacings for Cu_3Sn and Cu_6Sn_5 available in the literature [42, 43, 44, 45, 46, 47, 11]. Shang *et al.* [47, 46] have measured the lattice spacings of Cu and Cu_3Sn for several orientation pairs in SnBi/Cu solder joints. However, they have not measured the lattice spacings for Cu_6Sn_5 in the same

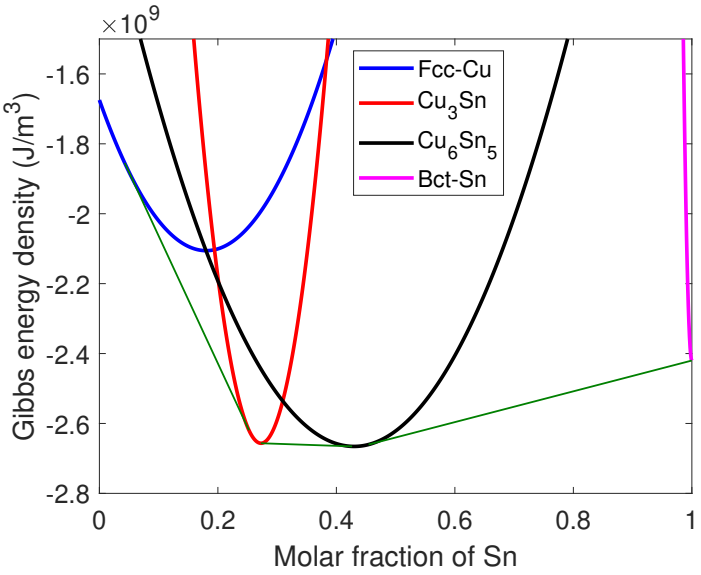

Figure 2: Parabolic functions fitted for Gibbs energy density showing the common tangents for the Fcc–Cu + Cu_3Sn, Cu_3Sn + Cu_6Sn_5 and Cu_6Sn_5 + Bct–Sn phase fields. A small solubility range is introduced for the intermetallic phases in order to drive the diffusion through these phases in phase-field simulations.

studies. There are other studies that measure the lattice spacings for Cu_6Sn_5 and Cu for different orientation pairs [42, 43, 44, 11]. However, they measure either at early stages of the intermetallic formation when Cu_3Sn has not formed [42, 45] or assuming hexagonal crystal structures for Cu_6Sn_5 and Cu_3Sn, as in the case of Panchenko *et al.* [11] and Suh *et al.* [43]. Furthermore, the lattice spacings change with temperature. There is thus no consistent set of experimental lattice spacing measurements for the orientation pairs in the Sn-Cu/Cu solder joint at 180 °C, which we consider as the annealing temperature in this study. Moreover, in this study, we consider the overall growth behavior of the, possibly polycrystalline, IMC layers, without considering the individual grains, each with a different crystal orientation, within the phases. Therefore, we choose the eigenstrains based on the molar volume change due to IMC formation. Furthermore, assuming an initially completely relaxed Cu-Sn joint, we take the eigenstrains in Fcc-Cu and Bct-Sn both equal to zero and the eigenstrains in Cu_3Sn and Cu_6Sn_5 as dilatational tensors based on the volume change associated with the formation of each IMC from the reference Cu-Sn structure. Though this does not accurately reflect the eigenstrains that would, in reality, arise from the crystallographic structures, this assumption considers an average volume change effect due to the

formation of the IMC without a detailed description of the polycrystal structure, that would require more accurate experimental data.

Using the TCSLD3 solder database from Thermo-Calc, which has descriptions of molar volume for different phases, we derive the dilatational eigenstrain in each IMC as $1/3 \times (V_m^{IMC} - s_1 V_m^{Cu} - s_2 V_m^{Sn})/(s_1 V_m^{Cu} + s_2 V_m^{Sn})$, where V_m^{IMC} is the molar volume of the IMC phase (Cu_3Sn or Cu_6Sn_5), s_1 and s_2 are the weighted stoichiometric coefficients of the IMC and V_m^{Cu} and V_m^{Sn} are the molar volumes of Fcc-Cu and Bct-Sn respectively. At 180 °C, we obtain the molar volumes from TCSLD3 database as $V_m^{Cu_3Sn} = 9.5490 \cdot 10^{-6}$ m^3, $V_m^{Cu_6Sn_5} = 1.0564 \cdot 10^{-5}$ m^3, $V_m^{Cu} = 7.3402 \cdot 10^{-6}$ m^3 and $V_m^{Sn} = 1.6554 \cdot 10^{-5}$ m^3. This gives a dilatational eigenstrain of -0.00327 in Cu_3Sn and -0.0279 in Cu_6Sn_5. This value for Cu_6Sn_5 is considerably higher than the value of -0.003 used by Hektor *et al.* [17]. Therefore, we do a parametric study for the eigenstrain of Cu_6Sn_5 with ~~four~~ **three** different sets of dilatational eigenstrains ($\epsilon_{kl}^{*,rho} = \epsilon^{*,rho} \times$ [1 1 0]) for the two phases: ~~(i) $\epsilon^{*,Cu_3Sn} = 0$, $\epsilon^{*,Cu_6Sn_5} = 0$,~~ ~~(ii)~~ **(i)** ϵ^{*,Cu_3Sn} = -0.00327, ϵ^{*,Cu_6Sn_5} = -0.0279, ~~(iii) (i)~~ **(ii)** ϵ^{*,Cu_3Sn} = -0.00327, ϵ^{*,Cu_6Sn_5} = -0.00327, and ~~(iv)~~ **(iii)** ϵ^{*,Cu_3Sn} = -0.00327, ϵ^{*,Cu_6Sn_5} = -0.001635.

3.5. Applied strains

To consider the effect of mechanical loading conditions, we perform simulations with and without applied strains. In Lin *et al.* [8], they study the effect of applying tensile and compressive strains of 2.5 % to the solder joint. We use the same value in our simulations with applied strains.

3.6. Parameters related to plastic deformation

Cu_3Sn and Cu_6Sn_5 are brittle and do not undergo plastic deformation. In experiments, the yield stress and hardening parameters are usually measured for the full solder joint. Therefore, limited data are available regarding individual phases, as required by the phase-field model. The yield stress measured by Deng *et al.* [48] using nanoindentation of a Sn-3.5Ag/Cu solder joint is used for the 4 phases: 180 ± 9 MPa for Fcc-Cu, 1787 ± 108 MPa for Cu_3Sn, 2009 ± 63 MPa for Cu_6Sn_5, and 35 ± 0.4 MPa for Bct-Sn. However, nanoindentation measurements of mechanical properties may give even larger errors of 20% due to pile-up effects, as discussed by Dimcic [49]. The hardening exponents for Cu and Sn are taken from

the work of Marques *et al.* [50], which uses nanoindentation to study the creep behaviour of Sn-Ag-Cu/Cu solder joints at 25 °C, as $n^{Fcc-Cu} = 12 \pm 7$ and $n^{Bct-Sn} = 7.8 \pm 3$. The scaling parameter is taken as $K^{Fcc-Cu} = K^{Bct-Sn} = 300$ MPa.

3.7. Diffusion and interface-related parameters

The following diffusion coefficients are used: $D^{\tilde{Fcc}-Cu} = 10^{-25}$ m^{2}s^{-1}, $D^{\tilde{Cu_3}Sn} = 4.04{\cdot}10^{-16}$ m^{2}s^{-1} , $D^{\tilde{Cu_6}Sn_5} = 1.12 \cdot 10^{-15}$ m^{2}s^{-1}, and $D^{\tilde{Bct}-Sn} = 10^{-14}$ m^{2}s^{-1}. For all phases except Bct-Sn, expressions from Mei *et al.* [51] at 180 °C are used. The value used for $D^{\tilde{Bct}-Sn}$ is lower than the value from Mei *et al.* to ensure that we can take a larger time step and achieve steady-state growth in a realistic time scale. Guan and Moelans [52] showed that this does not affect the intermetallic growth significantly.

For most cases, the parameters related to the interfacial energy are taken as: $\kappa = 2.25 \cdot 10^{-7}$ J m^{-1}, $\gamma = 1.5$, m $= 5 \cdot 10^6$ J m^{-3}. The interface mobility, L, is taken as $8 \cdot 10^{-13}$ m^3 N^{-1} s^{-1}. This gives an interfacial energy of 0.5 J m^{-2} and interfacial width of 3.3 Δx. It was verified that for these parameter values the growth-rate coefficients are reproduced with an error smaller than 1% in simulations for systems with planar interfaces [53, 34]. Grain boundary diffusion is not considered. For cases with eigenstrains based on volume change ('NoApp_VolEig', 'AppTensY_VolEig', 'AppCompY_VolEig', and 'AppCompX_VolEig', see section 3.9 and Table 1), $\kappa = 1.125 \cdot 10^{-7}$ J m^{-1} and m $= 10 \cdot 10^6$ J m^{-3} were taken. This was done in order to ensure the stability of the η profiles, while retaining the actual system size, interfacial energy and interfacial width (in terms of grid points) as in the other cases.

3.8. ab initio calculation of stiffness tensors

One of the key input parameters in this study is the stiffness of all phases. There is some experimental information available on the stiffnesses of pure Cu and Sn at low temperatures [54, 55]. However, the stiffnesses of the intermetallic phases Cu_3Sn and Cu_6Sn_5 are difficult to measure using tensile tests due to their brittle nature. There are some measurements of Young's modulus using compression tests [56] and micro- and nano-indentation [49], but since none of these phases is isotropic, we need measurements of the full stiffness tensor. *Ab initio* calculations have been performed [57, 58, 59, 60, 61] for Cu_3Sn and Cu_6Sn_5, however there is a large spread on the reported data and it is difficult to conclude on which values are

most accurate. Therefore, we have performed extra *ab initio* calculations for the 4 phases, with convergence criteria that are more severe than in any of the previous studies, to guide our selection of appropriate stiffness coefficients for the phase-field simulations.

The first-principles calculations were performed using Vienna Ab-initio Simulation Package (VASP 5.2 [62, 63, 64, 65]) at 0 K for pure Cu, Cu_3Sn, and pure Sn phases. Calculations for Cu_6Sn_5 were also attempted, however we were unable to make them converge due to the complex monoclinic crystal structure of Cu_6Sn_5 with large number of atoms in the unit cell. GGA-PBE approximation [66, 67] was used for the exchange-correlation functional with projected augmented wave potentials [68, 69]. Brillouin zones were sampled using Monkhorst-Pack [70] k-point meshes. The initial crystal structure files for Cu, Sn, and Cu_3Sn [71] were obtained from the Materials Project database [72, 73, 74, 75, 76]. Cu exists in a face-centred cubic structure with $Fm\overline{3}m$ space group (`https://materialsproject.org/materials/mp-30/`), Cu_3Sn in an orthorhombic structure with $Pmnm$ space group (`https://materialsproject.org/materials/mp-581786/`), and Sn in body-centred tetragonal structure with $I4_1/amd$ space group (`https://materialsproject.org/materials/mp-84/`). Different cut-off energies and k-point meshes were tested with the aim of obtaining a precision of 1 meV/atom for the energy calculation, compared to 0.01 eV/atom in previous calculations. The cut-off energy was then fixed at 414 eV and k-point meshes of $15 \times 15 \times 15$, $11 \times 14 \times 13$, and $12 \times 12 \times 22$ were used for Cu, Cu_3Sn, and Sn respectively. The system was allowed to relax till the energy converged to less than 10^{-7} eV/atom. Starting with the relaxed structure, the IBRION = 6 option in VASP was used to calculate the stiffness tensors. This option calculates the stress at different deformations applied to the system and derives the elastic constants. The results are discussed in Section 4.1.

3.9. Simulated cases

Simulations are performed considering elastic and plastic deformation until steady-state growth of the intermetallic phases is reached for all cases. In order to study the effects of eigenstrains and different loading conditions, we performed nine different simulations and we discuss the same divided into four different subsections: (i) no applied strains and the

eigenstrain in the IMCs varied ~~from zero to higher values~~ as described in Section 3.4, (ii) and (iii) the effect of applied strains in one direction with two different sets of eigenstrains, and finally (iv) the effect of loading direction. The full list of parameters that have been varied in each case and a short name for each case are provided in Table 1.

Table 1: List of simulation case studies with different sets of input parameters. Corresponding growth rates of IMCs in columns k_{Cu_3Sn} (m^2s^{-1}) and $k_{Cu_6Sn_5}$ (m^2s^{-1}).

Case	$\epsilon^{*,\mathbf{Cu_3Sn}}$	$\epsilon^{*,\mathbf{Cu_6Sn_5}}$	**Applied strain**	$\mathbf{k_{Cu_3Sn}}$ (m^2s^{-1})	$\mathbf{k_{Cu_6Sn_5}}$ (m^2s^{-1})
(i) Effect of eigenstrains with no applied strains (Section 4.2.1):					
~~NoApp_ZeroEig~~	~~0~~	~~0~~	~~[0 0 0]~~	~~$1.7021 \cdot 10^{-17}$~~	~~$4.4460 \cdot 10^{-17}$~~
NoApp_VolEig	-0.00327	-0.0279	[0 0 0]	~~3.4448~~ $\mathbf{3.44} \cdot 10^{-17}$	~~1.1261~~ $\mathbf{1.13} \cdot 10^{-17}$
NoApp_EqEig	-0.00327	-0.00327	[0 0 0]	~~1.7004~~ $\mathbf{1.70} \cdot 10^{-17}$	~~4.4521~~ $\mathbf{4.45} \cdot 10^{-17}$
NoApp_LowEig	-0.00327	-0.001635	[0 0 0]	~~1.6909~~ $\mathbf{1.69} \cdot 10^{-17}$	~~4.4767~~ $\mathbf{4.48} \cdot 10^{-17}$
(ii) Effect of applied strains with eigenstrains based on volume change (Section 4.2.2):					
NoApp_VolEig	-0.00327	-0.0279	[0 0 0]	~~3.4448~~ $\mathbf{3.44} \cdot 10^{-17}$	~~1.1261~~ $\mathbf{1.13} \cdot 10^{-17}$
AppTensY_VolEig	-0.00327	-0.0279	[0 0.025 0]	~~3.9599~~ $\mathbf{3.96} \cdot 10^{-17}$	~~2.1472~~ $\mathbf{2.15} \cdot 10^{-18}$
AppCompY_VolEig	-0.00327	-0.0279	[0 -0.025 0]	~~2.7687~~ $\mathbf{2.77} \cdot 10^{-17}$	~~1.3049~~ $\mathbf{1.30} \cdot 10^{-17}$
(iii) Effect of applied strains with equal eigenstrains (Section 4.2.3):					
NoApp_EqEig	-0.00327	-0.00327	[0 0 0]	~~1.7004~~ $\mathbf{1.70} \cdot 10^{-17}$	~~4.4521~~ $\mathbf{4.45} \cdot 10^{-17}$
AppTensY_EqEig	-0.00327	-0.00327	[0 0.025 0]	~~1.6351~~ $\mathbf{1.64} \cdot 10^{-17}$	~~3.9134~~ $\mathbf{3.91} \cdot 10^{-17}$
AppCompY_EqEig	-0.00327	-0.00327	[0 -0.025 0]	~~1.6773~~ $\mathbf{1.68} \cdot 10^{-17}$	~~3.6804~~ $\mathbf{3.68} \cdot 10^{-17}$
(iv) Effect of loading direction with eigenstrains based on volume change (Section 4.2.4):					
NoApp_VolEig	-0.00327	-0.0279	[0 0 0]	~~3.4448~~ $\mathbf{3.44} \cdot 10^{-17}$	~~1.1261~~ $\mathbf{1.13} \cdot 10^{-17}$
AppCompY_VolEig	-0.00327	-0.0279	[0 -0.025 0]	~~2.7687~~ $\mathbf{2.77} \cdot 10^{-17}$	~~1.3049~~ $\mathbf{1.30} \cdot 10^{-17}$
AppCompX_VolEig	-0.00327	-0.0279	[-0.025 0 0]	~~1.1325~~ $\mathbf{1.13} \cdot 10^{-16}$	$--$ (shrinks)

4. Results and discussion

4.1. ab initio calculations of stiffness tensors

Tables 2 and 3 show the values of stiffnesses from literature (both experimental measurements and *ab initio* calculations) and those calculated in the present study. The lattice parameters of the relaxed structures [53] from the calculations performed in the present study

were found to be: $a_{Cu} = b_{Cu} = c_{Cu} = 3.626$ Å, $a_{Cu_3Sn} = 5.537$ Å, $b_{Cu_3Sn} = 4.323$ Å, and $c_{Cu_3Sn} = 4.871$ Å, $a_{Sn} = b_{Sn} = 5.942$ Å, $c_{Sn} = 3.221$ Å. These are close to the experimentally reported values for Sn and other calculated values for Cu_3Sn and within the error bar of 1.1 $Å^2$/atom expected for the equilibrium unit cell volume [77]. There are intrinsic errors in the values obtained from *ab initio* calculations due to the exchange-correlation functional (E_{xc}) that is used. Lejaeghere *et al.* [77] have also shown that an error bar of 23 GPa is expected in the values of stiffness tensors calculated using GGA-PBE functional from a comparison of calculated values [78] for pure elements with experimental values. Taking this error into account, the values from the present study are close to the experimental values for the Cu phase as seen from Table 2. For Cu_3Sn, the values are similar to those of [59] and there is a large difference with the other calculated values from literature, even though An *et al.* [58] have used the same structure as that used in this work. Since there are no experimentally measured values for the stiffness of Cu_3Sn, we cannot comment further on the accuracy of the calculated values. For Sn, the use of LDA [61] seems to give stiffness values closer to the experimental values [55]. However, the values from the present work and from the work of Ghosh [61] using GGA are close to each other and, considering the error bar, are close to the experimental values. Moreover, the lattice parameters are better estimated by calculations from the present work compared to [61].

As input for the phase-field simulations, the experimentally measured stiffnesses of Cu [54] and Sn [55] are used. Since the stiffnesses calculated by *ab initio* in the present work for Cu and Sn match the experimental values well and we have ensured high accuracy for our calulations, we use the values at 0 K calculated in the present work for Cu_3Sn. These values are closest to those of [59]. For Cu_6Sn_5, the values from Chen *et al.* [57] and [60] are close to each other, especially when considering the reduced 2D version. We use the values from Chen *et al.* [57] for Cu_6Sn_5. At 300 K, the stiffness of Cu drops by about 5% [54] and that of Sn by about 10–15% [55]; however, these are neglected since we do not have any information about the temperature dependence of the stiffnesses of Cu_3Sn and Cu_6Sn_5. Moreover, the orientation dependence of the elastic constants is also not taken into account. Since the phase-field simulations will be performed in 2D, the reduced 2D version of the elastic constants at 0 K for Cu, Cu_3Sn, Cu_6Sn_5, and Sn (extrapolated from experimental

measurement) were derived assuming plane strain conditions.

Table 2: Stiffness tensors (GPa) (only non-zero components listed) and lattice parameters of Fcc-Cu and Cu_3Sn from literature and present work

Parameter	Cu	Cu	Cu_3Sn	Cu_3Sn	Cu_3Sn	Cu_3Sn
C_{1111}	176.2±0.2%	176	205	207	155	158
C_{2222}	176.2±0.2%	176	164	226	174	183
C_{3333}	176.2±0.2%	176	219	194	148	128
C_{2323}	0	0	61	58	50	52
C_{1313}	0	0	64	47	44	36
C_{1212}	81.77±0.25%	94	39	57	55	57
C_{1122}	124.94±0.44%	113	94	93	79	82
C_{1133}	124.94 ± 0.44%	113	106	94	76	86
C_{2233}	124.94±0.44%	113	106	94	95	101
Method	experiment	*ab initio*	*ab initio*	*ab initio*	*ab initio*	*ab initio*
Temperature	Extrapolated to 0 K	0 K	0 K	0 K	0 K	0 K
Crystal structure	Not measured	FCC	Orthorhombic *Cmcm* 80 atoms	Orthorhombic *Pmmn* 8 atoms	Orthorhombic *Pmmn* 8 atoms	Orthorhombic *Pmmn* 8 atoms
Lattice parameters (a, b, c) (Å)	Not determined	3.626, 3.626, 3.626	Not reported	5.429, 4.267, 4.666	5.618, 4.367, 4.835	5.537, 4.323, 4.871
Cut-off energy (eV)	NA	414	–	580	400	414
k-points	NA	15 × 15 × 15	–	8 × 10 × 9	–	11 × 14 × 13
E_{xc}	NA	GGA-PBE	GGA-PBE	GGA-PBE	GGA-PW91	GGA-PBE
Reference	[54]	Present work	[57]	[58]	[59]	Present work

Table 3: Stiffness tensors (GPa) (only non-zero components listed) and lattice parameters of Cu_6Sn_5 and Bct-Sn from literature and present work

Parameter	Cu_6Sn_5	Cu_6Sn_5	Sn	Sn	Sn	Sn
C_{1111}	169	156	82.74±0.62	84	63	60
C_{2222}	165	165	82.74±0.62	84	63	60
C_{3333}	186	156	103.10±0.77	104	80	79
C_{2323}	46	42	26.95±0.21	25	20	20
C_{1313}	54	52	26.95±0.21	25	20	20
C_{1212}	46	48	28.18±0.21	28	23	24
C_{1122}	69	62	57.85±1.15	62	51	50
C_{1133}	67	69	34.21±1.1	35	26	33
C_{2233}	67	61	34.21±1.1	35	26	32
C_{1113}	17	-11	0	0	0	0
C_{2213}	34	17	0	0	0	0
C_{3313}	28	6	0	0	0	0
C_{2312}	-3	7	0	0	0	0
Method	*ab initio*	*ab initio*	experiment	*ab initio*	*ab initio*	*ab initio*
Temperature	0 K	0 K	4.2 K	0 K	0 K	0 K
Crystal structure	Monoclinic *C2/c* 44 atoms	Monoclinic *C2/c* 44 atoms	Not determined	Tetragonal	Tetragonal	Tetragonal $I4_1/amd$
Lattice parameters (a, b, c) (Å)	Not reported	10.848, 7.130, 9.643	5.812, 5.812, 3.157	4.3383, 4.3383, 2.3583	4.4734, 4.4734, 2.4286	5.942, 5.942, 3.221
Cut-off energy (eV)	–	320	NA	314	314	414
k-points	–	16 (irreducible)	NA	–	–	12 × 12 × 22
E_{xc}	GGA-PBE	GGA-PBE	NA	LDA-CA	GGA-PW91	GGA-PBE
Reference	[57]	[60]	[55]	[61]	[61]	Present work

4.2. Simulation of intermetallic growth in Sn–Cu/Cu solder joints

Since this is the first time that the coupled elastic and plastic deformation models used in this study are implemented in a multi-phase framework, we verified that the elastic and viscoplastic energy densities interpolate linearly across the interfaces. A short discussion on this is provided in Appendix E.

For all cases where the eigenstrains are non-zero, the von Mises stress exceeds the yield stress in the Fcc-Cu and/or the Bct-Sn phase; therefore, it is necessary to consider both elastic and plastic deformation for simulating intermetallic growth with the set of parameters used in this study. For example, Figure 3 shows the von Mises stress profiles for cases 'AppCompY_VolEig' at t = 1000 s and 100100 s (Figure 3a) and 'AppCompY_EqEig' at t = 1000 s and 500100 s (Figure 3b). For both cases, as expected, the von Mises stress in Fcc-Cu and Bct-Sn reduce with time as plastic strain evolves.

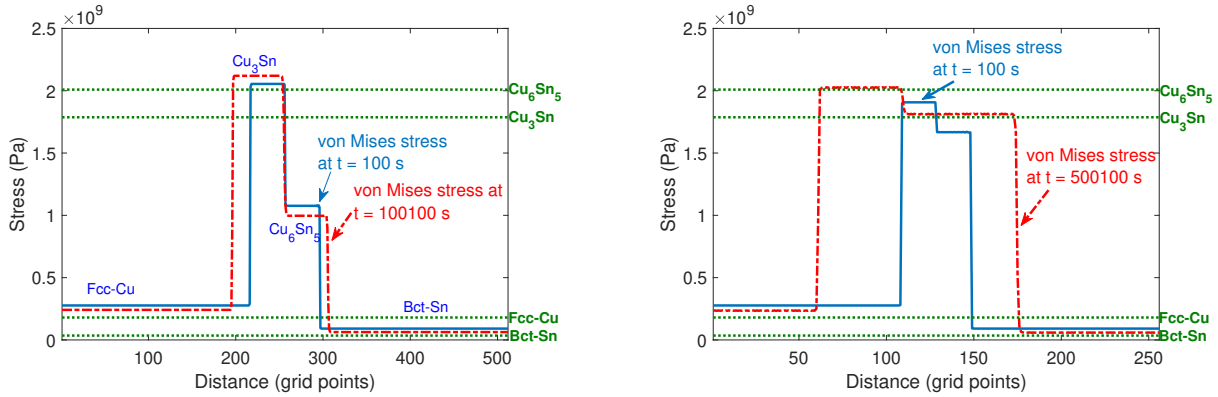

Figure 3: The von Mises stresses at times (a) t = 1000 s and 100100 s for case (a) 'AppCompY_VolEig' at times (b) t = 1000 s and 500100 s for case 'AppCompY_EqEig': these illustrate that the von Mises stress exceeds the yield stress (shown in dotted green lines for each phase) and it is therefore necessary to consider both elastic and plastic deformation. This is also true for all cases with non-zero eigenstrains. The phases present in the simulations are Fcc-Cu, Cu_3Sn, Cu_6Sn_5 and Bct-Sn from left to right (indicated only in (a) for readability).

The growth of the intermetallic phases is assumed to be diffusion-controlled and the most commonly reported relation is a parabolic time dependence at steady-state [79]:

$$d = d_0 + \sqrt{kt} \tag{11}$$

where d = thickness of the layer at time t, d_0 the initial thickness, and k the growth-rate coefficient. In this study, we fit the widths with the parabolic relation taking the steady-state region as the duration from 20 to 44 h or 72000 to 158400 s (corresponding to 268.33 to 397.99 $s^{1/2}$), since the phase-field variables become fully diffuse only after an initial period of time and, moreover, there is an initial transient region in which parabolic growth kinetics are not observed. For the case 'AppTensY_VolEig' alone, the fitting is done from 268.33 $s^{1/2}$ to 331.81 $s^{1/2}$, which is the latest available result. The k values for both Cu_3Sn and Cu_6Sn_5 for all cases are also listed in Table 1 and will be discussed further in the following subsections.

4.2.1. Effect of eigenstrains with no applied strains

Firstly, to study the effect of eigenstrains on the growth rates without the effect of applied strain, we consider ~~four~~ **three** cases as listed in Table 1. For all cases, there are no externally applied strains, which implies that the average total strain is zero. ~~The first case 'NoApp_ZeroEig' is equivalent to considering no mechanical deformation since the eigenstrains are zero and there are no applied strains also.~~ As a parametric study, we have chosen three cases, with the eigenstrain value for Cu_6Sn_5 varying across the three cases and the value for Cu_3Sn fixed at -0.00327 (based on volume change). The three cases are 'NoApp_VolEig', where the eigenstrain of Cu_6Sn_5 is also determined based on volume change (= -0.0279), 'NoApp_EqEig', where equal eigenstrains of -0.00327 are used for both phases, and 'NoApp_LowEig', where the eigenstrain in Cu_6Sn_5 = -0.0016325, which is half of the value in Cu_3Sn. Figure 4 shows the growth kinetics of all cases with no applied strains. All cases show parabolic IMC growth after an initial transient regime.

The cases 'NoApp_EqEig' and 'NoApp_LowEig' **show very similar growth kinetics**. ~~are very similar to the first case with zero eigenstrains, showing that there is not a significant effect on the growth kinetics with the choice of eigenstrains for these two cases~~. **However, f**~~F~~or 'NoApp_VolEig' case, the growth rate is significantly different from ~~all~~ **the** other **two** cases. ~~considered in this subsection.~~ The growth of Cu_3Sn is accelerated and that of Cu_6Sn_5 is decelerated compared to other cases. As seen from Table 1, k_{Cu_3Sn} for 'NoApp_VolEig' is over twice the value for other cases and $k_{Cu_6Sn_5}$ is about four times smaller than the value for

the other cases. The much higher value of eigenstrain in Cu_6Sn_5 in this case clearly changes the growth rates significantly. **This shows that the IMC growth kinetics can change with the magnitude of eigenstrains present in the system**.

Figure 4c shows the composition profiles for all cases at time t $\approx$ 100000 s and the initial composition profile at t = 0, which is the same for all cases. There is a composition gradient across the IMCs as diffusion occurs through them and the IMCs grow. There seems to be no significant effect of the strains on the composition of the IMCs.

Previous experimental measurements of the growth coefficient k [80, 81, 79, 82, 49] which do not consider any effect of applied strains range from ~~$4.2025 \cdot 10^{-18}$~~ $\mathbf{4.20 \cdot 10^{-18}}$ to ~~$7.4304 \cdot 10^{-17}$~~ $\mathbf{7.43 \cdot 10^{-17}}$ m^2s^{-1} for Cu_3Sn and ~~$1.0693 \cdot 10^{-17}$~~ $\mathbf{1.07 \cdot 10^{-17}}$ to ~~$1.7424 \cdot 10^{-16}$~~ $\mathbf{1.74 \cdot 10^{-16}}$ m^2s^{-1} for Cu_6Sn_5 respectively. Though these studies do not explicitly consider the influence of strains in the system, there will always be some internal strains present due to lattice mismatch and the resulting eigenstrains. The growth coefficients for all ~~four~~ **three** cases considered in the present work fall within this rather wide range from experiments. In general, Cu_6Sn_5 has a much higher growth rate than Cu_3Sn as thicker layers of Cu_6Sn_5 are observed in experiments. This is true for all simulation cases except 'NoApp_VolEig', where $k_{Cu_6Sn_5}$ is less than k_{Cu_3Sn}, which is due to the higher eigenstrain in Cu_6Sn_5 compared to the other cases. We thereby establish that the choice of eigenstrain is very important in the IMC growth kinetics and through simulations, we can study the effects of eigenstrains independently unlike experiments where there are a large number of parameters that can change simultaneously.

4.2.2. Effect of applied strains with eigenstrains based on volume change

Next, we consider the effect of applied strains on the growth rates. With the eigenstrains fixed to values based on volume change for the two IMCs, we consider three cases: 'NoApp_VolEig', a reference case with no applied strains, 'AppTensY_VolEig', with applied tensile strain of 2.5% in the y direction, and 'AppCompY_VolEig', with an applied compressive strain of 2.5% in the y direction. Figure 5 shows the growth kinetics for all three cases. All cases show parabolic IMC growth after an initial transient period when there are applied strains also. We stopped the 'AppTensY_VolEig' at around 110000 s since the strains became

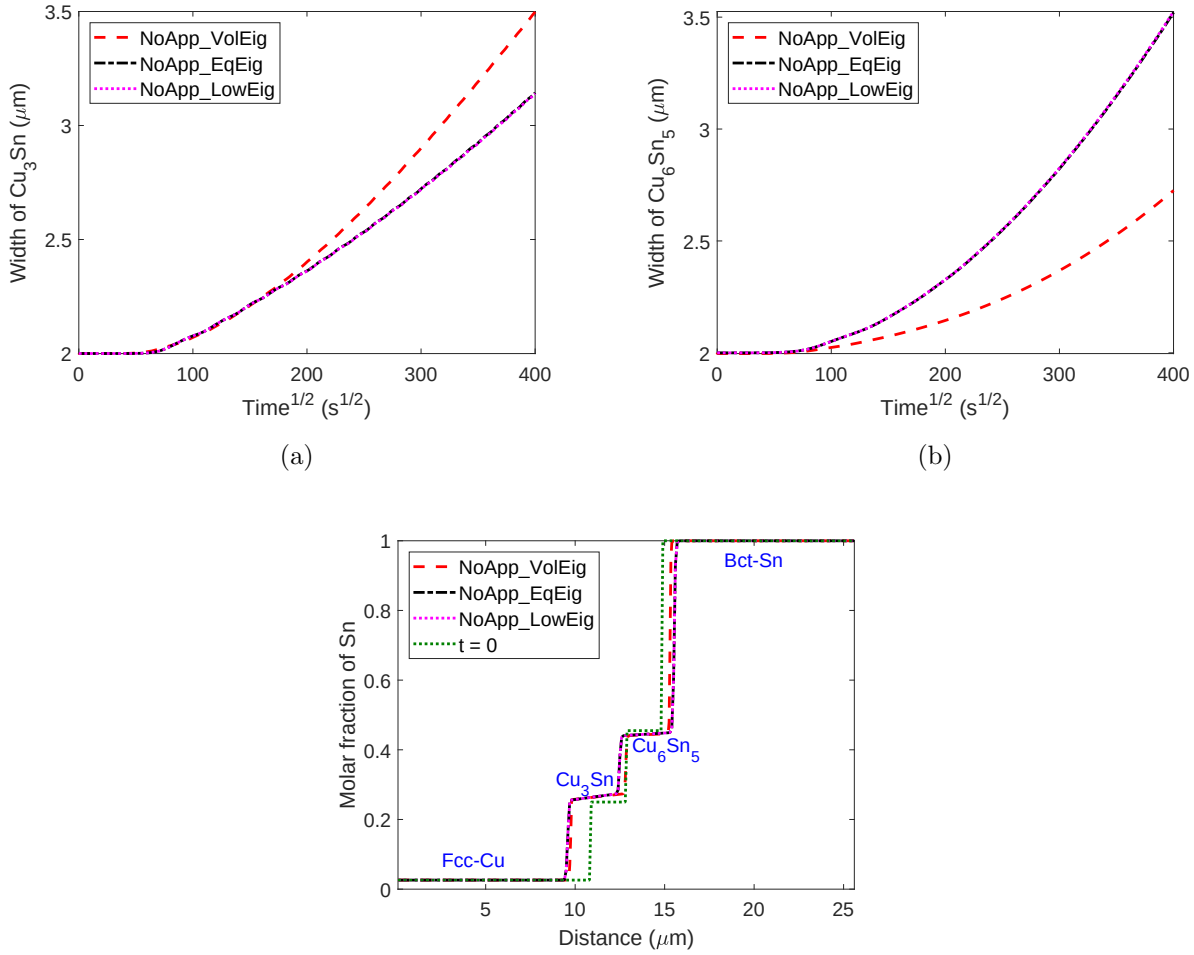

Figure 4: Simulation results of intermetallic layer growth at 180 °C considering the effect of eigenstrains when there are no applied strains: (a) Cu_3Sn and (b) Cu_6Sn_5 layer width show parabolic growth kinetics for all cases and the eigenstrains based on volume change show significant effect on the growth; (c) Composition profiles at t ≈ 100000 s compared to the initial composition, showing no significant effect of eigenstrains.

too high at the interface between Cu_6Sn_5n and Bct-Sn and the small strain limit would not hold any further.

There is an increase in the growth rate of Cu_3Sn in case of applied tensile strain but a decrease in the case of applied compressive strain. The trend is reversed for Cu_6Sn_5, where there is a significant decrease (over five times smaller k) in growth rate in the case of applied tensile strain and a small increase in the case of applied compressive strain. The corresponding values of k may be found in Table 1.

Figure 5c shows the composition profiles for all cases at t ≈ 100000 s. There is a small drop in the composition of Cu_6Sn_5 for the case 'AppCompY_VolEig', but overall there is no significant effect of applied strains on the phase compositions.

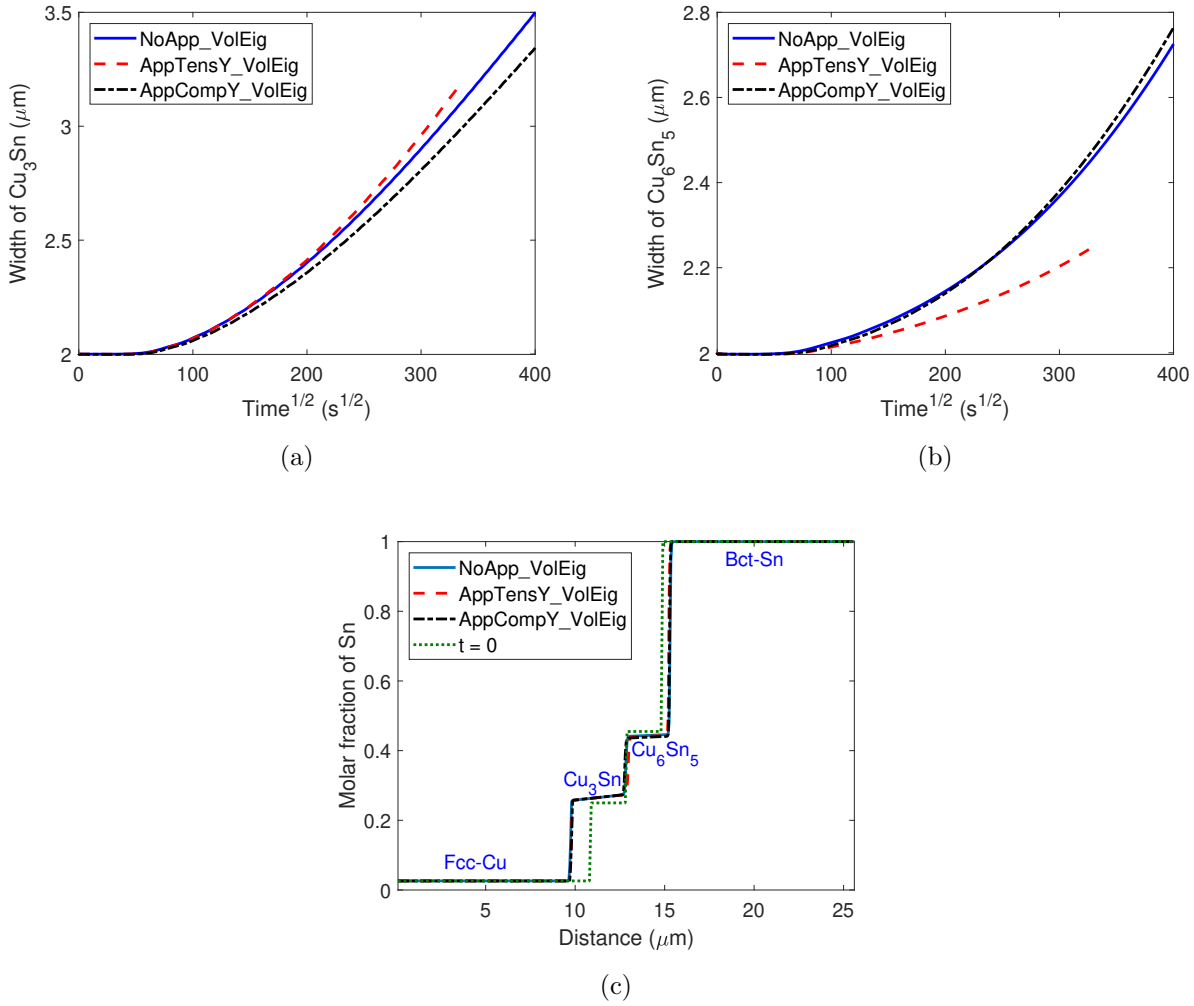

Figure 5: Simulation results of intermetallic layer growth at 180 °C considering the effect of applied strains with eigenstrains based on volume change: (a) Cu_3Sn and (b) Cu_6Sn_5 layer width show parabolic growth kinetics for all cases and there is a clear effect of applied strains on growth kinetics; (c) Composition profiles at ≈ 100000 s compared to the initial composition.

In order to investigate further the effect of the applied strains, Figure 6 shows the profiles of elastic energy density (6a), von Mises stress (6b), viscoplastic energy density (6c), and cumulative plastic strain (6d) at time t = 100100 s for all cases. The high value of elastic energy density for 'AppTensY_VolEig' can be directly correlated to the decreased growth rate

of Cu_6Sn_5 compared to the case of no applied strains. In the case of 'AppCompY_VolEig', the elastic energy in Cu_3Sn is highest among all phases and there is a corresponding decrease in the growth rate compared to the case of no applied strains. Plastic deformation in Fcc-Cu and Bct-Sn correspond to the von Mises stress profile. The magnitude of plastic deformation is highest in the case of compressive applied strain. Figure 6b also shows that the von Mises stress in the IMCs is higher than the yield stress for some conditions and this shows that there is a likelihood of brittle fracture to occur in the IMCs in these cases. This is in line with the observations of Lin *et al.* where they observe a lot of cracks in Cu_6Sn_5.

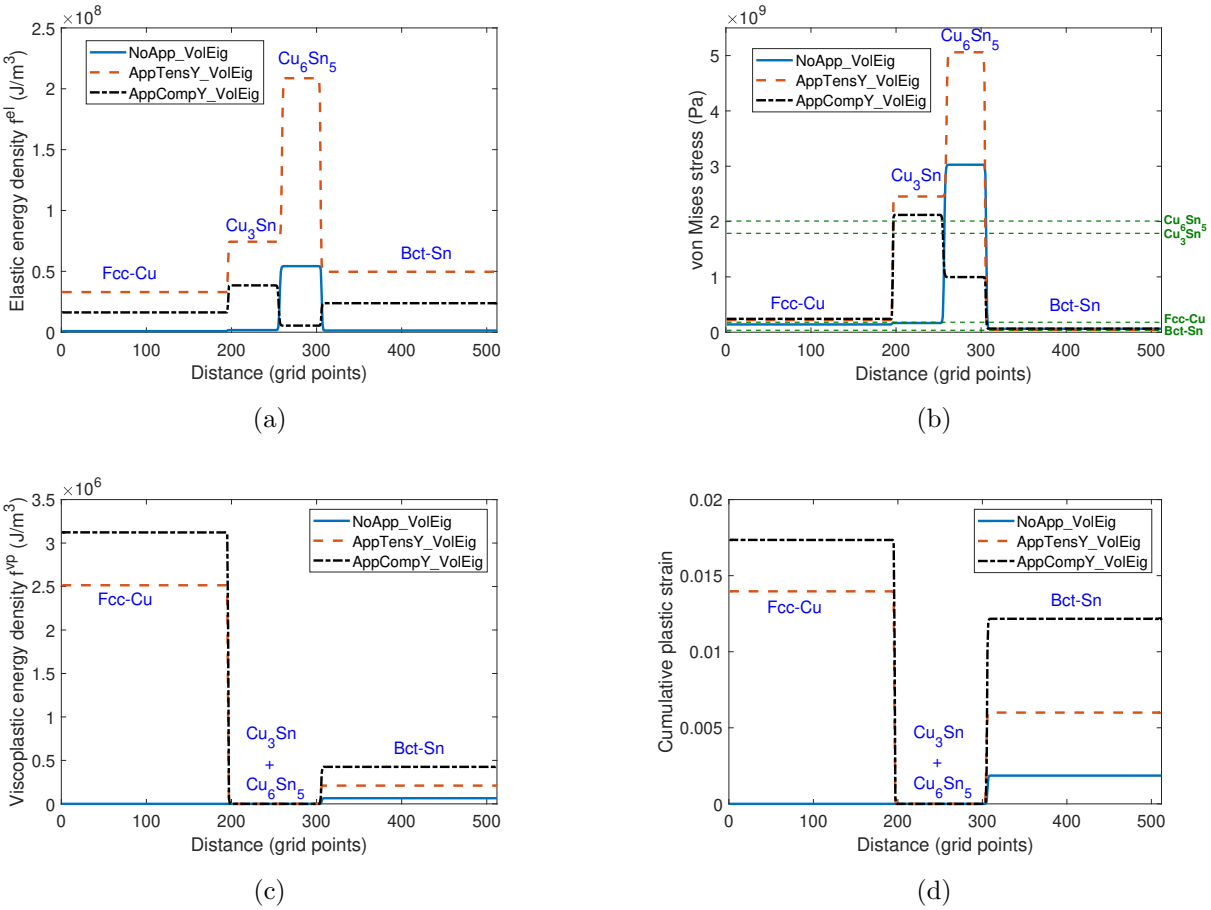

Figure 6: Simulation results of intermetallic layer growth at 180 °C considering the effect of applied strains with eigenstrains based on volume change: (a) Elastic energy densities, (b) von Mises stress (yield stress of each phase shown in green dotted lines), (c) Viscoplastic energy density, and (d) Cumulative plastic strain at t = 100100 s for all cases. The high elastic energy in Cu_6Sn_5 for 'AppTensY_VolEig' leads to decrease in growth rate and the plastic deformation follows the von Mises stress profile.

An applied strain of 2.5% is chosen in this work similar to the experimental study of Lin *et al.* [8]. They have performed experiments on Sn/Cu layers with applied tensile and compressive strains of 2.5% at 200 °C. They observe that the Cu_3Sn layer shows accelerated growth with tensile strain and decelerated growth with compressive strain. For Cu_6Sn_5, there is accelerated growth for both types of applied strains, but there is a steep increase when the strain is compressive. In our simulations, we observe a similar trend for Cu_3Sn and for Cu_6Sn_5 for applied compressive strain, though the change is small, but for Cu_6Sn_5 with applied tensile strain, the growth is decelerated significantly. Therefore in the next section, simulations with applied strains are presented using a smaller eigenstrain value for Cu_6Sn_5 to analyze how eigenstrain affects the growth rate under applied loading conditions.

4.2.3. Effect of applied strains with equal eigenstrains

In order to further study the effect of applied strains, we perform simulations with another set of eigenstrains (= -0.00327 in both IMCs). Here again, we consider three different cases: 'NoApp_EqEig', a reference case with no applied strains, 'AppTensY_EqEig', with applied tensile strain of 2.5% in the y direction, and 'AppCompY_EqEig', with an applied compressive strain of 2.5% in the y direction. Figure **7** shows the growth kinetics for all three cases. All cases show parabolic IMC growth after an initial transient period when there are applied strains for this set of eigenstrains also.

As shown in Table 1, there is a small decrease in the growth rates of both Cu_3Sn and Cu_6Sn_5 for both applied tensile and compressive strains for this case.

Figure 7c shows the composition profiles for all cases at t $\approx$ 100000 s and there is no difference between all cases as expected.

Figure 7d shows the elastic energy densities at t = 100000 s for all cases. The magnitude of the energies are much lesser than those in Section 4.2.2 and therefore, the effect of strains on the growth kinetics is small.

Some trends from Lin *et al.* [8] were similar for the cases considered in Section 4.2.2, but for the cases considered in the current section, only the decelerated growth with compressive strain for Cu_3Sn is similar to the experimental trends. On the other hand, the growth rates of Cu_6Sn_5 are smaller than those of Cu_3Sn for all cases in Section 4.2.2, whereas in the

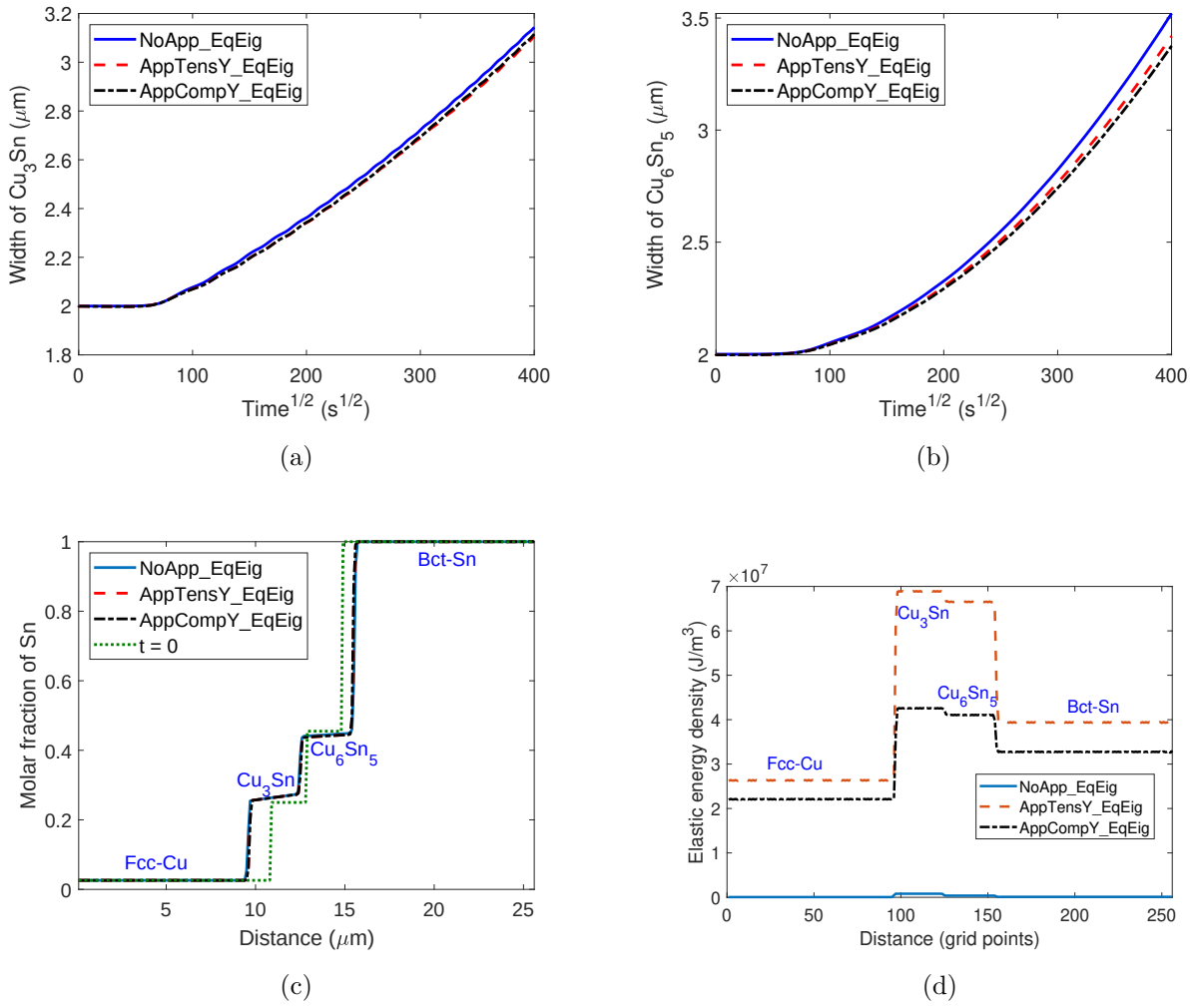

Figure 7: Simulation results of intermetallic layer growth at 180 °C considering the effect of applied strains with equal eigenstrains: (a) Cu_3Sn and (b) Cu_6Sn_5 layer width show parabolic growth kinetics for all cases and there is an effect of applied strain on the growth rate; (c) Composition profiles at t $\approx$ 100000 s compared to the initial composition; (d) Elastic energy densities at t = 100000 s.

current section, the growth rates of Cu_6Sn_5 are larger than those of Cu_3Sn for all cases. The latter is in better agreement with experimental observations [8] where the Cu_6Sn_5 layer is always found to be thicker than the Cu_3Sn layer.

4.2.4. Effect of loading direction with eigenstrains based on volume change

Finally, we also perform simulations to show the effect of the loading direction on IMC growth. We consider three cases for discussion in this section, while fixing the eigenstrains

to values based on volume change: 'NoApp_VolEig', reference case with no applied strains, 'AppCompY_VolEig', with applied compressive strain in the y direction, and finally, 'AppCompX_VolEig', with applied compressive strain in the x direction.

Figure 8 shows the growth kinetics for all three cases. When the direction of applied compressive strain changes from y to x, Cu_6Sn_5 starts to shrink immediately. This clearly shows the importance of loading direction on the intermetallic growth. Moreover, this also indicates that the phase equilibria shift in the presence of strains. Figure 8c shows the composition profiles of all cases at t $\approx$ 100000 s (t = 108100 s for case 'AppCompX_VolEig'). We see that the composition of Cu_6Sn_5 changes and has almost disappeared for case 'AppCompX_VolEig'. Also, a less steep composition gradient has developed at the interface between Cu_6Sn_5 and Bct–Sn. Figure 8d shows that the elastic energy density in Cu_6Sn_5 is much higher than in the other phases, which could explain why it shrinks. Since the effect of loading direction is not clearly discussed in any experimental work to the best of our knowledge, we need further investigation from both experiments and simulations to understand the effect of the loading direction.

From this study on the effect of different eigenstrains and applied strains, we can conclude that strains play an important role in intermetallic growth in Sn-Cu/Cu solder joints. In addition to explaining some of the experimental observations, the power of these simulations lies in their ability to obtain insights on different coupled effects which cannot be isolated or controlled in experiments and which are, nevertheless, important for understanding this type of microstructure evolution. Further experimental validation is required on the effect of applied strains which were studied in this work. This approach can also be used to study the effect of morphology by considering an initial multi-grain structure. Furthermore, we can extend this approach to multi-component systems to simulate IMC growth in higher order systems like Sn-Ag-Cu/Cu solder joints.

5. Conclusions

We formulated and validated a quantitative multi-phase phase-field model taking into account elastic and plastic deformation. This was applied to the growth of intermetallic layers formed in a Sn-Cu/Cu solder joint during solid-state ageing at 180 °C. We performed

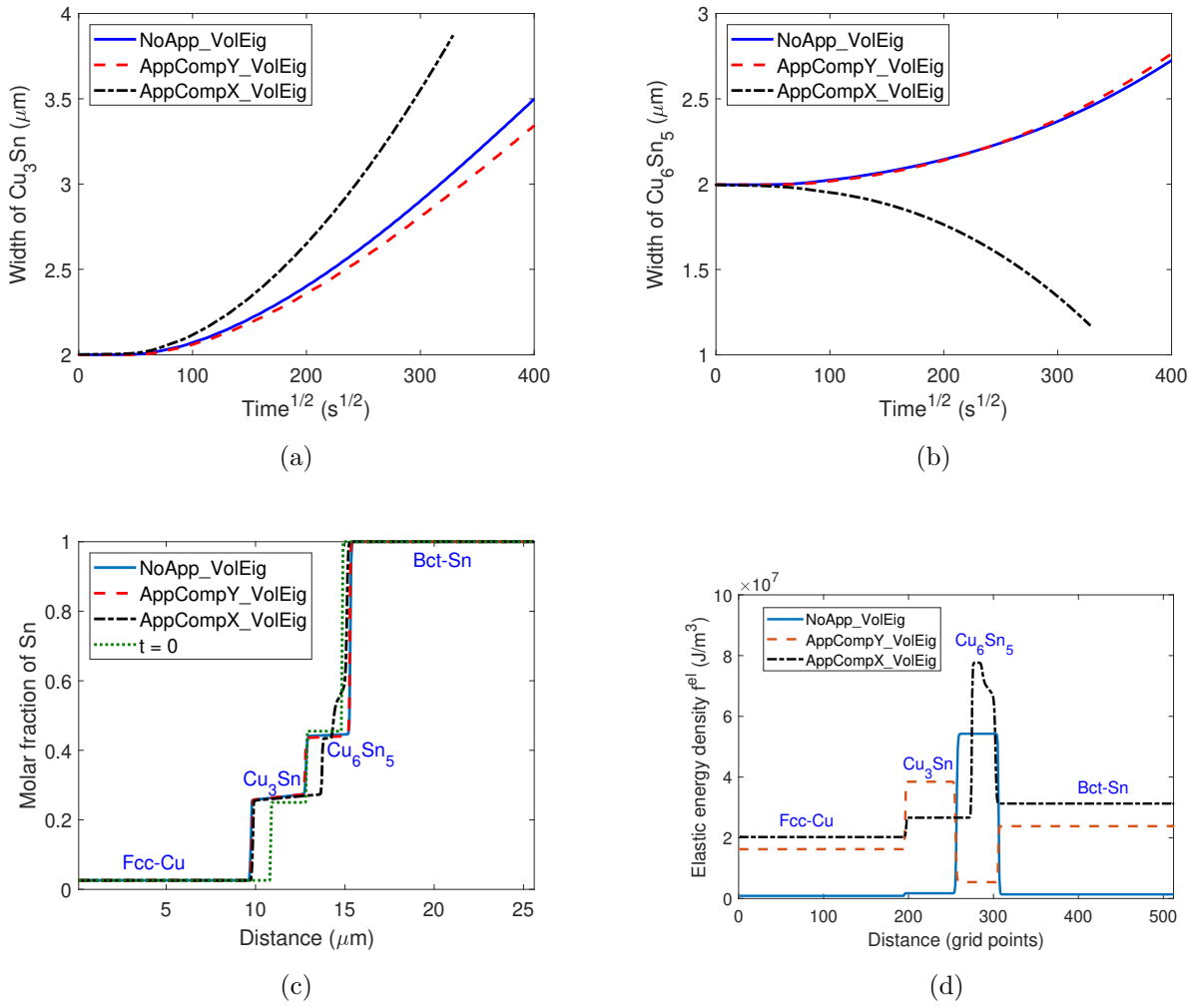

Figure 8: Simulation results of intermetallic layer growth at 180 °C considering the effect of loading direction with eigenstrains based on volume change: (a) Cu_3Sn and (b) Cu_6Sn_5 layer width: change in loading direction to x from y forces the Cu_6Sn_5 to shrink due to high elastic energy (d); (c) Composition profiles at t ≈ 100000 s compared to the initial composition: phase equilibria changes with loading direction; (d) Elastic energy densities at t = 100000 s

a parametric study with different values of eigenstrains and externally applied strains. When no externally applied strains are considered (but considering the elastic and plastic effects due to eigenstrains, which are inherently present in experiments), the growth rates from our simulations fall within the wide range of the corresponding experimentally measured growth rates reported in the literature. Some observations from experiments with regard to the effect of external loading of the joint on the IMC growth, were reproduced in the simulations. The

simulations show that, not only the magnitude of the external loading, but also the loading conditions (i.e. tensile or compressive) and its direction with respect to the joint, has an influence on the growth behavior of the IMCs. However, further experiments are required to validate the effect of applied strains shown in this work. Though not clearly established by experimental studies so far, it is worth to mention that all simulations where the IMCs grow, showed parabolic growth kinetics at steady-state even when mechanical deformation was included, as it is normally expected for diffusion controlled growth. Moreover, our study showed that the growth behaviour of the IMC phases and the effect of externally applied strains in the simulations is sensitive to the used eigenstrain values. This urges the need for more accurate eigenstrain values. Finally, and most importantly, through these simulations, we were able to study and clearly isolate the effect of eigenstrains, applied strains and the loading direction on the IMC growth rates, which can guide more focused future experimental work.

References

[1] M. Abtew, G. Selvaduray, Lead-free solders in microelectronics, Materials Science and Engineering: R: Reports 27 (2000) 95–141.

[2] J. Glazer, Microstructure and mechanical properties of Pb-free solder alloys for low-cost electronic assembly: a review, Journal of Electronic Materials 23 (1994) 693–700.

[3] T. An, F. Qin, Effects of the intermetallic compound microstructure on the tensile behavior of Sn3.0Ag0.5Cu/Cu solder joint under various strain rates, Microelectronics Reliability 54 (2014) 932–938.

[4] S. Cheng, C.-M. Huang, M. Pecht, A review of lead-free solders for electronics applications, Microelectronics Reliability 75 (2017) 77–95.

[5] H. R. Kotadia, P. D. Howes, S. H. Mannan, A review: On the development of low melting temperature Pb-free solders, Microelectronics Reliability 54 (2014) 1253–1273.

[6] G. Zeng, S. Xue, L. Zhang, L. Gao, W. Dai, J. Luo, A review on the interfacial

intermetallic compounds between sn–ag–cu based solders and substrates, Journal of Materials Science: Materials in Electronics 21 (2010) 421–440.

[7] S. Annuar, R. Mahmoodian, M. Hamdi, K.-N. Tu, Intermetallic compounds in 3D integrated circuits technology: a brief review, Science and Technology of advanced MaTerialS 18 (2017) 693–703.

[8] C.-P. Lin, C.-M. Chen, Y.-W. Yen, Enhanced growth of the Cu_6Sn_5 phase in the Sn/Ag/Cu and Sn/Cu multilayers subjected to applied strain, Journal of Alloys and Compounds 591 (2014) 297–303.

[9] O. M. Abdelhadi, L. Ladani, Effect of joint size on microstructure and growth kinetics of intermetallic compounds in solid-liquid interdiffusion Sn3.5Ag/Cu-substrate solder joints, Journal of Electronic Packaging 135 (2013) 021004.

[10] C.-P. Lin, C.-M. Chen, C.-H. Lin, W.-C. Su, Interfacial reactions of Sn/Ag/Cu tri-layer on a deformed polyimide substrate, Journal of Alloys and Compounds 502 (2010) L17–L19.

[11] I. Panchenko, Process-dependent Microstructure Changes in Solid-Liquid Interdiffusion Interconnects for 3D Integration ed. Wolter, Klaus J and Zerna, Thomas and Detert, Markus, volume 20 of *System Integration in Electronic Packaging*, Detert, Markus, 2014.

[12] M. Park, S. Gibbons, R. Arróyave, Phase-field simulations of intermetallic compound evolution in Cu/Sn solder joints under electromigration, Acta Materialia 61 (2013) 7142–7154.

[13] M. Park, R. Arróyave, Early stages of intermetallic compound formation and growth during lead-free soldering, Acta Materialia 58 (2010) 4900–4910.

[14] M. Park, R. Arróyave, Concurrent nucleation, formation and growth of two intermetallic compounds (Cu_6Sn_5 and Cu_3Sn) during the early stages of lead-free soldering, Acta Materialia 60 (2012) 923–934.

[15] H. Xiong, Z. Huang, Effects of stress and electromigration on microstructural evolution in microbumps of three-dimensional integrated circuits, Transactions on Device and Materials Reliability (2014).

[16] R. L. J. M. Ubachs, Thermomechanical modelling of microstructure evolution in solder alloys, Ph.D. thesis, Technische Universiteit Eindhoven, 2005.

[17] J. Hektor, M. Ristinmaa, H. Hallberg, S. Hall, S. Iyengar, Coupled diffusion-deformation multiphase field model for elastoplastic materials applied to the growth of Cu6Sn5, Acta Materialia 108 (2016) 98–109.

[18] A. Durga, P. Wollants, N. Moelans, Evaluation of interfacial excess contributions in different phase-field models for elastically inhomogeneous systems, Modelling and Simulation in Materials Science and Engineering 21 (2013) 055018.

[19] E. Chason, N. Jadhav, W. Chan, L. Reinbold, K. Kumar, Whisker formation in Sn and Pb-Sn coatings: Role of intermetallic growth, stress evolution, and plastic deformation processes, Applied Physics Letters 92 (2008) 171901.

[20] F. Haddadi, Rapid intermetallic growth under high strain rate deformation during high power ultrasonic spot welding of aluminium to steel, Materials & Design 66 (2015) 459–472.

[21] A. Gaubert, Y. Le Bouar, A. Finel, Coupling phase field and viscoplasticity to study rafting in Ni-based superalloys, Philosophical Magazine 90 (2010) 375–404.

[22] X. Guo, S.-Q. Shi, X. Ma, Elastoplastic phase field model for microstructure evolution, Applied Physics Letters 87 (2005) 221910.

[23] A. Gaubert, A. Finel, Y. Le Bouar, G. Boussinot, Viscoplastic phase field modelling of rafting in Ni base superalloys, Continuum Models and Discrete Systems CMDS11 (2008) 161–166.

[24] M. Cottura, Y. Le Bouar, A. Finel, B. Appolaire, K. Ammar, S. Forest, A phase field model incorporating strain gradient viscoplasticity: Application to rafting in Ni-base superalloys, Journal of the Mechanics and Physics of Solids 60 (2012) 1243–1256.

[25] H. K. Yeddu, A. Malik, J. Ågren, G. Amberg, A. Borgenstam, Three-dimensional phase-field modeling of martensitic microstructure evolution in steels, Acta Materialia 60 (2012) 1538–1547.

[26] A. Yamanaka, T. Takaki, Y. Tomita, Elastoplastic phase-field simulation of self-and plastic accommodations in cubic → tetragonal martensitic transformation, Materials Science and Engineering: A 491 (2008) 378–384.

[27] C. Herrmann, E. Schoof, D. Schneider, F. Schwab, A. Reiter, M. Selzer, B. Nestler, Multiphase-field model of small strain elasto-plasticity according to the mechanical jump conditions, Computational Mechanics (2018) 1–14.

[28] E. Borukhovich, P. Engels, T. Böhlke, O. Shchyglo, I. Steinbach, Large strain elasto-plasticity for diffuse interface models, Modelling and Simulation in Materials Science and Engineering 22 (2014) 034008.

[29] M. Cottura, B. Appolaire, A. Finel, Y. Le Bouar, Coupling the phase field method for diffusive transformations with dislocation density-based crystal plasticity: Application to Ni-based superalloys, Journal of the Mechanics and Physics of Solids 94 (2016) 473–489.

[30] A. Durga, P. Wollants, N. Moelans, A quantitative phase-field model for two-phase elastically inhomogeneous systems, Computational Materials Science 99 (2015) 81–95.

[31] D. Schneider, O. Tschukin, A. Choudhury, M. Selzer, T. Böhlke, B. Nestler, Phase-field elasticity model based on mechanical jump conditions, Computational Mechanics 55 (2015) 887–901.

[32] O. Tschukin, D. Schneider, B. Nestler, An elasto-chemical phase-field model for isotropic solids, European Journal of Mechanics-A/Solids (2018).

[33] J. Eiken, B. Böttger, I. Steinbach, Multiphase-field approach for multicomponent alloys with extrapolation scheme for numerical application, Physical Review E 73 (2006) 066122.

[34] N. Moelans, A quantitative and thermodynamically consistent phase-field interpolation function for multi-phase systems, Acta Materialia 59 (2011) 1077–1086.

[35] D. Ananthanarayanan, Development of an Elastoplastic Phase-field Model for Multi-phase Systems, Ph.D. thesis, KU Leuven, 2015.

[36] S. Hu, L. Chen, A phase-field model for evolving microstructures with strong elastic inhomogeneity, Acta Materialia 49 (2001) 1879–1890.

[37] A. Dinsdale, A. Watson, A. Kroupa, J. Vřešťál, A. Zemanová, J. Vízdal, et al., COST Action 531 - Atlas of phase diagrams for lead-free soldering, volume 1, COST Office, Brussels, Belgium, 2008.

[38] K.-W. Moon, W. Boettinger, U. Kattner, F. Biancaniello, C. Handwerker, Experimental and thermodynamic assessment of Sn-Ag-Cu solder alloys, Journal of Electronic Materials 29 (2000) 1122–1136.

[39] B. Sundman, J. Ågren, A regular solution model for phases with several components and sublattices, suitable for computer applications, Journal of Physics and Chemistry of Solids 42 (1981) 297–301.

[40] J.-O. Andersson, T. Helander, L. Höglund, P. Shi, B. Sundman, Thermo-Calc & DICTRA, computational tools for materials science, Calphad 26 (2002) 273–312.

[41] R. Shi, N. Ma, Y. Wang, Predicting equilibrium shape of precipitates as function of coherency state, Acta Materialia 60 (2012) 4172–4184.

[42] K.-K. Wang, D. Gan, K.-C. Hsieh, S.-Y. Chiou, The microstructure of η'-Cu_6Sn_5 and its orientation relationships with Cu in the early stage of growth, Thin Solid Films 518 (2010) 1667–1674.

[43] J. Suh, K. Tu, N. Tamura, A synchrotron radiation x-ray microdiffraction study on orientation relationships between a Cu_6Sn_5 and Cu substrate in solder joints, JOM 58 (2006) 63–66.

[44] H. Zou, H. Yang, Z. Zhang, Morphologies, orientation relationships and evolution of Cu_6Sn_5 grains formed between molten Sn and Cu single crystals, Acta Materialia 56 (2008) 2649–2662.

[45] P. Shang, Z. Liu, D. Li, J. K. Shang, Tem observations of the growth of intermetallic compounds at the SnBi/Cu interface, Journal of Electronic Materials 38 (2009) 2579.

[46] P. Shang, Z. Liu, X. Pang, D. Li, J. K. Shang, Growth mechanisms of Cu_3Sn on polycrystalline and single crystalline Cu substrates, Acta Materialia 57 (2009) 4697–4706.

[47] P. Shang, Z. Liu, D. Li, J. K. Shang, Bi-induced voids at the Cu_3Sn/Cu interface in eutectic SnBi/Cu solder joints, Scripta Materialia 58 (2008) 409–412.

[48] X. Deng, N. Chawla, K. Chawla, M. Koopman, Deformation behavior of (Cu, Ag)–Sn intermetallics by nanoindentation, Acta Materialia 52 (2004) 4291–4303.

[49] B. Dimcic, Characterization of materials for low temperature bonding of miniaturized interconnects, Ph.D. thesis, KU Leuven, Belgium, 2014.

[50] V. Marques, B. Wunderle, C. Johnston, P. Grant, Nanomechanical characterization of Sn–Ag–Cu/Cu joints – Part 2: Nanoindentation creep and its relationship with uniaxial creep as a function of temperature, Acta Materialia 61 (2013) 2471–2480.

[51] Z. Mei, A. Sunwoo, J. Morris, Analysis of low-temperature intermetallic growth in copper-tin diffusion couples, Metallurgical Transactions A 23 (1992) 857–864.

[52] Y. Guan, N. Moelans, Influence of the solubility range of intermetallic compounds on their growth behavior in hetero-junctions, Journal of Alloys and Compounds 635 (2015) 289–299.

[53] Y. Guan, Development of a Method to Determine the Solubility Ranges of Intermetallic Compounds in Metal-metal Connections, Ph.D. thesis, KU Leuven, 2015.

[54] W. Overton Jr, J. Gaffney, Temperature variation of the elastic constants of cubic elements. I. Copper, Physical Review 98 (1955) 969.

[55] J. Rayne, B. Chandrasekhar, Elastic constants of β tin from 4.2 K to 300 K, Physical Review 120 (1960) 1658.

[56] L. Jiang, H. Jiang, N. Chawla, The Effect of Crystallographic Orientation on the Mechanical Behavior of Cu_6Sn_5 by Micropillar Compression Testing, Journal of Electronic Materials 41 (2012) 2083–2088.

[57] J. Chen, Y.-S. Lai, Towards elastic anisotropy and strain-induced void formation in Cu–Sn crystalline phases, Microelectronics Reliability 49 (2009) 264–268.

[58] R. An, C. Wang, Y. Tian, H. Wu, Determination of the elastic properties of Cu_3Sn through first-principles calculations, Journal of Electronic Materials 37 (2008) 477–482.

[59] X. Pang, S. Wang, L. Zhang, Z. Liu, J. Shang, First principles calculation of elastic and lattice constants of orthorhombic Cu_3Sn crystal, Journal of Alloys and Compounds 466 (2008) 517–520.

[60] N. Lee, V. Tan, K. Lim, First-principles calculations of structural and mechanical properties of Cu_6Sn_5, Applied Physics Letters 88 (2006) 031913–031913.

[61] G. Ghosh, First-principles calculation of phase stability and cohesive properties of Ni-Sn intermetallics, Metallurgical and Materials Transactions A 40 (2009) 4–23.

[62] G. Kresse, J. Hafner, Ab initio molecular dynamics for liquid metals, Physical Review B 47 (1993) 558.

[63] G. Kresse, J. Hafner, Ab initio molecular-dynamics simulation of the liquid-metal–amorphous-semiconductor transition in germanium, Physical Review B 49 (1994) 14251.

[64] G. Kresse, J. Furthmüller, Efficiency of ab-initio total energy calculations for metals and semiconductors using a plane-wave basis set, Computational Materials Science 6 (1996) 15–50.

[65] G. Kresse, J. Furthmüller, Efficient iterative schemes for ab initio total-energy calculations using a plane-wave basis set, Physical Review B 54 (1996) 11169.

[66] J. P. Perdew, K. Burke, M. Ernzerhof, Generalized gradient approximation made simple, Physical Review Letters 77 (1996) 3865.

[67] J. P. Perdew, K. Burke, M. Ernzerhof, Erratum: Generalized gradient approximation made simple, Physical Review Letters 78 (1997) 1396.

[68] P. E. Blöchl, Projector augmented-wave method, Physical Review B 50 (1994) 17953.

[69] G. Kresse, D. Joubert, From ultrasoft pseudopotentials to the projector augmented-wave method, Physical Review B 59 (1999) 1758.

[70] H. J. Monkhorst, J. D. Pack, Special points for Brillouin-zone integrations, Physical Review B 13 (1976) 5188.

[71] W. Burkhardt, K. Schubert, Ueber messingartige Phasen mit A3-verwandter Struktur, Zeitschrift fuer Metallkunde 50 (1959) 442–452.

[72] A. Jain, S. P. Ong, G. Hautier, W. Chen, W. D. Richards, S. Dacek, S. Cholia, D. Gunter, D. Skinner, G. Ceder, K. A. Persson, The Materials Project: A materials genome approach to accelerating materials innovation, APL Materials 1 (2013) 011002.

[73] Materials Project, ???? URL: `http://www.materialsproject.org`.

[74] E. Owen, E. Yates, Precision measurements of crystal parameters, Philosophical Magazine, Serie 6 (1901-1925) 15 (1933) 472–487.

[75] G. Bergerhoff, R. Hundt, R. Sievers, I. Brown, The inorganic crystal structure data base, Journal of Chemical Information and Computer Sciences 23 (1983) 66–69.

[76] F. Karlsruhe, Inorganic Crystal Structure Database, ???? URL: `http://icsd.fiz-karlsruhe.de`.

[77] K. Lejaeghere, V. Van Speybroeck, G. Van Oost, S. Cottenier, Error estimates for solid-state density-functional theory predictions: an overview by means of the ground-state elemental crystals, Critical Reviews in Solid State and Materials Sciences 39 (2014) 1–24.

[78] S. Shang, A. Saengdeejing, Z. Mei, D. Kim, H. Zhang, S. Ganeshan, Y. Wang, Z. Liu, First-principles calculations of pure elements: Equations of state and elastic stiffness constants, Computational Materials Science 48 (2010) 813–826.

[79] M. Onishi, H. Fujibuchi, Reaction-diffusion in the Cu-Sn system, Transactions JIM 16 (1975) 539–547.

[80] Y. M. Kim, H.-R. Roh, S. Kim, Y.-H. Kim, Kinetics of intermetallic compound formation at the interface between Sn-3.0Ag-0.5Cu solder and Cu-Zn alloy substrates, Journal of Electronic Materials 39 (2010) 2504–2512.

[81] A. Paul, C. Ghosh, W. Boettinger, Diffusion parameters and growth mechanism of phases in the Cu-Sn system, Metallurgical and Materials Transactions A 42 (2011) 952–963.

[82] M. Pawelkiewicz, J. Janczak-Rusch, K. Sosnowska, M. Danielewski, Handbook of High–Temperature Lead-Free Solders, Volume 3: Group Project Reports ed. A. Kroupa, COST, Brussels, 2012.

[83] N. Moelans, A. Durga, Phase-field study of IMC growth in SnCu/Cu solder joints including elastoplastic effects – data sets and codes, Mendeley Data, V1, (2019). doi:10.17632/pkb252vtps.1.

[84] N. Moelans, B. Blanpain, P. Wollants, Quantitative analysis of grain boundary properties in a generalized phase field model for grain growth in anisotropic systems, Physical Review B 78 (2008) 024113.

[85] N. Moelans, B. Blanpain, P. Wollants, Quantitative phase-field approach for simulating grain growth in anisotropic systems with arbitrary inclination and misorientation dependence, Physical Review Letters 101 (2008) 025502.

[86] A. G. Khachaturyan, Theory of structural transformations in solids, Wiley, New York, 1983.

[87] I. Steinbach, M. Apel, Multi phase field model for solid state transformation with elastic strain, Physica D: Nonlinear Phenomena 217 (2006) 153–160.

[88] K. Ammar, B. Appolaire, G. Cailletaud, S. Forest, Combining phase field approach and homogenization methods for modelling phase transformation in elastoplastic media, European Journal of Computational Mechanics/Revue Européenne de Mécanique Numérique 18 (2009) 485–523.

[89] W. C. Johnson, Precipitate shape evolution under applied stress - thermodynamics and kinetics, Metallurgical Transactions A 18 (1987) 233–247.

Acknowledgements

The authors thank Yuanyuan Guan, Stefaan Cottenier and Danny Vanpoucke for their support with setting up the *ab initio* calculations. The authors thank OT/07/040, CREA/12/012 and European Research Council (ERC) under the European Union's Horizon 2020 research and innovation programme (grant agreement n 714754 INTERDIFSION ERC-2016-STG), for financial support. Simulations were performed using the VSC Flemish Supercomputer Center, funded by the Hercules foundation and the Flemish Government department EWI. This work was carried out within the framework of COST MP0602 Advanced Solder Materials for High Temperature Application.

Code and data availability

The codes used to generate the data and the simulation data for this project are stored in a public repository [83].

Appendix A. Different contributions to the free energy

Appendix A.1. Chemical energy

The chemical energy density is defined using the interpolation function (1) as:

$$f^{ch} = \sum_{\rho=1}^{N} \phi_\rho f^{ch,\rho} = \sum_{\rho=1}^{N} \phi_\rho \frac{G_{\rho,m}(c)}{V_m}, \tag{A.1}$$

where $G_{\rho,m}$ is the molar Gibbs energy of phase ρ and V_m a constant value related to the molar volume. A constant molar volume value of 10^{-5} m^3 mol^{-1} is assumed for all phases. Volume changes due to phase transformations are taken into account through the eigenstrain in the elastic part of the free energy. Phase compositions c_ρ are introduced:

$$c = \sum_{\rho=1}^{N} \phi_\rho c_\rho, \tag{A.2}$$

which are determined by assuming local chemical equilibrium at every point, i. e. , the diffusion potentials are assumed to be equal in all the coexisting phases of all components:

$$\frac{\partial f^{ch,\alpha}}{\partial c_\alpha} = \frac{\partial f^{ch,\beta}}{\partial c_\beta} = ... = \frac{\partial f^{ch,\rho}}{\partial c_\rho} = \tilde{\mu}. \tag{A.3}$$

Appendix A.2. Interfacial energy

The interfacial energy density according to Moelans *et al.* [84, 85] is formulated as:

$$f^{int} = m f_0(\boldsymbol{\eta}) + \frac{\kappa}{2} \sum_{\rho}^{N} (\nabla \eta_\rho)^2, \tag{A.4}$$

where f_0 is a multi-well potential. The full form of f_0 is given as a fourth-order Landau polynomial in the order parameters:

$$f_0(\boldsymbol{\eta}) = \sum_{\rho=1}^{N} \left[\frac{\eta_\rho^4}{4} - \frac{\eta_\rho^2}{2} \right] + \gamma \sum_{\rho=1}^{N} \sum_{\sigma>\rho}^{N} \eta_\rho^2 \eta_\sigma^2 + \frac{1}{4}. \tag{A.5}$$

γ, κ, and m are taken as constants and determine, together with f_0, the specific interfacial energy and the diffuse interface width [84].

Appendix A.3. Elastic energy

The elastic strain energy density is interpolated as:

$$f^{el} = \sum_{\rho=1}^{N} \phi_\rho f^{el,\rho}. \tag{A.6}$$

The elastic energy is formulated using the scheme proposed by the authors ([30]). In this study, it is extended to multi-phase systems and plastic deformation is also considered.

The elastic energy according to Hooke's law is:

$$f^{el,\rho} = \frac{1}{2} \epsilon_{ij}^{el,\rho} C_{ijkl}^{\rho} \epsilon_{kl}^{el,\rho} \tag{A.7}$$

where $\epsilon_{ij}^{el,\rho}$ is the elastic strain in ρ and C_{ijkl}^{ρ} is the stiffness of phase ρ. The elastic strain is defined as: $\epsilon_{ij}^{el,\rho} = \overline{\epsilon_{ij}} + \delta\epsilon_{ij}^{el,\rho} - \epsilon_{ij}^{*,\rho} - \epsilon_{ij}^{pl,\rho}$, where $\overline{\epsilon_{ij}}$ is the applied strain, $\delta\epsilon_{ij}^{el,\rho}$ the local heterogeneous strain and $\epsilon_{ij}^{*,\rho}$ the eigenstrain, and $\epsilon_{ij}^{pl,\rho}$ the plastic strain [86]. The total strain is given by $\epsilon_{ij}^{\rho} = \overline{\epsilon_{ij}} + \delta\epsilon_{ij}^{\rho}$.

In a reduced 2D version, we take into consideration the local equilibrium at the interfaces (interface normal direction: 1 and parallel direction: 2) where σ_{11} and σ_{12} components of the stress are equal in the two phases and the total strain ϵ_{22} is equal in the two phases.

σ_{11} and σ_{12} are then calculated using Steinbach-Apel's scheme [87], since it uses the Reuss-Sachs condition of equal stresses at the interfaces. Therefore, in our scheme, the stress components $\sigma_{11}^{\rho} = \sigma_{11}^{SAS}$, $\sigma_{12}^{\rho} = \sigma_{12}^{SAS}$.

ϵ_{22} is calculated using Voigt-Taylor's scheme [88] since it uses the equal total strain condition at the interfaces. Therefore, in our scheme, the total strain component $\epsilon_{22}^{\rho} = \epsilon_{22}^{VTS}$. From this, the elastic strains are calculated as: $\epsilon_{22}^{el,VTS,\rho} = \epsilon_{22}^{VTS} - \epsilon_{22}^{*,\rho} - \epsilon_{22}^{pl,\rho}$.

The unknown components σ_{22}^{ρ}, $\epsilon_{11}^{el,\rho}$ and $\epsilon_{12}^{el,\rho}$ are formulated as follows:

$$\sigma_{22}^{\rho} = C_{1122}^{\rho}\epsilon_{11}^{el,\rho} + C_{2222}^{\rho}\epsilon_{22}^{el,VTS,\rho} + 2C_{2212}^{\rho}\epsilon_{12}^{\rho}, \tag{A.8}$$

$$\epsilon_{11}^{el,\rho} = S_{1111}^{\rho}\sigma_{11}^{SAS} + S_{1122}^{\rho}\sigma_{22}^{\rho} + 2S_{1112}^{\rho}\sigma_{12}^{SAS}, \tag{A.9}$$

$$\epsilon_{12}^{el,\rho} = S_{1112}^{\rho}\sigma_{11}^{SAS} + S_{2212}^{\rho}\sigma_{22}^{\rho} + 2S_{1212}^{\rho}\sigma_{12}^{SAS}. \tag{A.10}$$

σ_{22}^{ρ} can be calculated in terms of σ_{11}^{SAS}, σ_{12}^{SAS} and $\epsilon_{22}^{el,VTS,\rho}$ as

$$\begin{aligned}\sigma_{22}^{\rho} = {} & \frac{C_{1122}^{\rho}(S_{1111}^{\rho}\sigma_{11}^{SAS} + 2S_{1112}^{\rho}\sigma_{12}^{SAS}) + C_{2222}^{\rho}\epsilon_{22}^{el,VTS,\rho}}{1 - C_{1122}^{\rho}S_{1122}^{\rho} - 2C_{2212}^{\rho}S_{2212}^{\rho}} \\ & + \frac{2C_{2212}^{\rho}(S_{1112}^{\rho}\sigma_{11}^{SAS} + 2S_{1212}^{\rho}\sigma_{12}^{SAS})}{1 - C_{1122}^{\rho}S_{1122}^{\rho} - 2C_{2212}^{\rho}S_{2212}^{\rho}}.\end{aligned} \tag{A.11}$$

$\epsilon_{11}^{el,\rho}$ and $\epsilon_{12}^{el,\rho}$ may also be computed similarly using Equations (A.9)–(A.10).

The elastic energy is given by:

$$f^{el} = \sum_{\alpha}^{N} \phi_{\alpha} f^{el,\alpha} \tag{A.12}$$

$$= \sum_{\alpha}^{N} \frac{1}{2}\phi_{\alpha}(\sigma_{11}^{SAS}\epsilon_{11}^{el,\alpha} + \sigma_{22}^{\alpha}\epsilon_{22}^{el,VTS,\alpha} + \sigma_{12}^{SAS}\epsilon_{12}^{el,\alpha}) \tag{A.13}$$

The elastic driving force for microstructural evolution, $\frac{\partial f^{el}}{\partial \eta_\alpha}$, is related to $\frac{\partial f^{el}}{\partial \phi_\alpha}$ (see Appendix B), which is calculated as:

$$\frac{\partial f^{el}}{\partial \phi_\alpha} = f^{el,\alpha} + \phi_\alpha \frac{\partial f^{el,\alpha}}{\partial \phi_\alpha} + \sum_{\rho \neq \alpha} \phi_\rho \frac{\partial f^{\rho,el}}{\partial \phi_\alpha}, \tag{A.14}$$

$$\begin{aligned} &= f^{\alpha,el} + \frac{1}{2}\phi_\alpha \left[\frac{\partial \sigma_{11}^{SAS,}}{\partial \phi_\alpha} \epsilon_{11}^{el,\alpha} + \sigma_{11}^{SAS,} \frac{\partial \epsilon_{11}^{el,\alpha}}{\partial \phi_\alpha} + \frac{\partial \sigma_{22}^{\alpha}}{\partial \phi_\alpha} \epsilon_{22}^{el,\alpha,VTS} \right] \\ &+ \frac{1}{2}\phi_\alpha \left[\frac{\partial \sigma_{12}^{SAS}}{\partial \phi_\alpha} \epsilon_{12}^{el,\alpha} + \sigma_{12}^{SAS} \frac{\partial \epsilon_{12}^{el,\alpha}}{\partial \phi_\alpha} \right] \\ &+ \frac{1}{2} \sum_{\rho \neq \alpha} \phi_\rho \left[\frac{\partial \sigma_{11}^{SAS}}{\partial \phi_\alpha} \epsilon_{11}^{el,\rho} + \sigma_{11}^{SAS} \frac{\partial \epsilon_{11}^{el,\rho}}{\partial \phi_\alpha} + \frac{\partial \sigma_{22}^{\rho}}{\partial \phi_\alpha} \epsilon_{22}^{el,VTS,\rho} \right] \\ &+ \frac{1}{2} \sum_{\rho \neq \alpha} \phi_\rho \left[\frac{\partial \sigma_{12}^{SAS}}{\partial \phi_\alpha} \epsilon_{12}^{el,\rho} + \sigma_{12}^{SAS} \frac{\partial \epsilon_{12}^{el,\rho}}{\partial \phi_\alpha} \right], \end{aligned} \tag{A.15}$$

since $\epsilon_{22}^{el,VTS,\alpha}$ is a constant with respect to all ϕ. The partial stress and strain derivatives are fully derived in Appendix C.

For 3D systems, a similar approach as given in [30] may be followed, which includes all the stress and strain components.

Appendix B. Calculation of driving forces for microstructure evolution

$$\frac{\partial f^{el}}{\partial \eta_{\rho i}} = \sum_{\sigma \neq \rho} \frac{\partial f^{el}}{\partial \phi_\sigma} \frac{\partial \phi_\sigma}{\partial \eta_{\rho i}} + \frac{\partial f^{el}}{\partial \phi_\rho} \frac{\partial \phi_\rho}{\partial \eta_{\rho i}} \tag{B.1}$$

$$= -\frac{2\eta_{\rho i}}{\sum_\alpha |\eta_\alpha|^2} \sum_{\sigma \neq \rho} \phi_\sigma \frac{\partial f^{el}}{\partial \phi_\sigma} + \frac{2\eta_{\rho i}}{\sum_\alpha |\eta_\alpha|^2} (1 - \phi_\rho) \frac{\partial f^{el}}{\partial \phi_\rho} \tag{B.2}$$

$$= \frac{2\eta_{\rho i}}{\sum_\alpha |\eta_\alpha|^2} \left[\frac{\partial f^{el}}{\partial \phi_\rho} - \sum_\sigma \phi_\sigma \frac{\partial f^{el}}{\partial \phi_\sigma} \right] \tag{B.3}$$

Appendix C. Calculation of strain and stress derivatives for elastic driving force

The partial derivatives are given as:

$$\frac{\partial \sigma_{22}^{\alpha}}{\partial \phi_{\alpha}} = \frac{C_{1122}^{\alpha}(S_{1111}^{\alpha}\frac{\partial \sigma_{11}^{SAS}}{\partial \phi_{\alpha}} + 2S_{1112}^{\alpha}\frac{\partial \sigma_{12}^{SAS}}{\partial \phi_{\alpha}})}{1 - C_{1122}^{\alpha}S_{1122}^{\alpha} - 2C_{2212}^{\alpha}S_{2212}^{\alpha}} + \frac{2C_{2212}^{\alpha}(S_{1112}^{\alpha}\frac{\partial \sigma_{11}^{SAS}}{\partial \phi_{\alpha}} + 2S_{1212}^{\alpha}\frac{\partial \sigma_{12}^{SAS}}{\partial \phi_{\alpha}})}{1 - C_{1122}^{\alpha}S_{1122}^{\alpha} - 2C_{2212}^{\alpha}S_{2212}^{\alpha}} \tag{C.1}$$

$$\frac{\partial \sigma_{22}^{\alpha}}{\partial \phi_{\rho}} = \frac{C_{1122}^{\alpha}(S_{1111}^{\alpha}\frac{\partial \sigma_{11}^{SAS}}{\partial \phi_{\rho}} + 2S_{1112}^{\alpha}\frac{\partial \sigma_{12}^{SAS}}{\partial \phi_{\rho}})}{1 - C_{1122}^{\alpha}S_{1122}^{\alpha} - 2C_{2212}^{\alpha}S_{2212}^{\alpha}} + \frac{2C_{2212}^{\alpha}(S_{1112}^{\alpha}\frac{\partial \sigma_{11}^{SAS}}{\partial \phi_{\rho}} + 2S_{1212}^{\alpha}\frac{\partial \sigma_{12}^{SAS}}{\partial \phi_{\rho}})}{1 - C_{1122}^{\alpha}S_{1122}^{\alpha} - 2C_{2212}^{\alpha}S_{2212}^{\alpha}} \tag{C.2}$$

$$\frac{\partial \epsilon_{11}^{\alpha}}{\partial \phi_{\alpha}} = S_{1111}^{\alpha}\frac{\partial \sigma_{11}^{SAS}}{\partial \phi_{\alpha}} + S_{1122}^{\alpha}\frac{\partial \sigma_{22}^{\alpha}}{\partial \phi_{\alpha}} + 2S_{1112}^{\alpha}\frac{\partial \sigma_{12}^{SAS}}{\partial \phi_{\alpha}} \tag{C.3}$$

$$\frac{\partial \epsilon_{12}^{\alpha}}{\partial \phi_{\alpha}} = S_{1112}^{\alpha}\frac{\partial \sigma_{11}^{SAS}}{\partial \phi_{\alpha}} + S_{2212}^{\alpha}\frac{\partial \sigma_{22}^{\alpha}}{\partial \phi_{\alpha}} + 2S_{1212}^{\alpha}\frac{\partial \sigma_{12}^{SAS}}{\partial \phi_{\alpha}} \tag{C.4}$$

$$\frac{\partial \epsilon_{11}^{\alpha}}{\partial \phi_{\rho}} = S_{1111}^{\alpha}\frac{\partial \sigma_{11}^{SAS}}{\partial \phi_{\rho}} + S_{1122}^{\alpha}\frac{\partial \sigma_{22}^{\alpha}}{\partial \phi_{\rho}} + 2S_{1112}^{\alpha}\frac{\partial \sigma_{12}^{SAS}}{\partial \phi_{\rho}} \tag{C.5}$$

$$\frac{\partial \epsilon_{12}^{\alpha}}{\partial \phi_{\rho}} = S_{1112}^{\alpha}\frac{\partial \sigma_{11}^{SAS}}{\partial \phi_{\rho}} + S_{2212}^{\alpha}\frac{\partial \sigma_{22}^{\alpha}}{\partial \phi_{\rho}} + 2S_{1212}^{\alpha}\frac{\partial \sigma_{12}^{SAS}}{\partial \phi_{\rho}} \tag{C.6}$$

$$\frac{\partial \sigma_{11}^{SAS,\alpha'}}{\partial \phi_{\alpha}} = C_{1111}^{\alpha'}\frac{\partial \epsilon_{11}^{SAS,\alpha'}}{\partial \phi_{\alpha}} + C_{1122}^{\alpha'}\frac{\partial \epsilon_{22}^{SAS,\alpha'}}{\partial \phi_{\alpha}} + 2C_{1112}^{\alpha'}\frac{\partial \epsilon_{12}^{SAS,\alpha'}}{\partial \phi_{\alpha}} \tag{C.7}$$

$$\frac{\partial \sigma_{12}^{SAS,\alpha'}}{\partial \phi_{\alpha}} = C_{1112}^{\alpha'}\frac{\partial \epsilon_{11}^{SAS,\alpha'}}{\partial \phi_{\alpha}} + C_{2212}^{\alpha'}\frac{\partial \epsilon_{22}^{SAS,\alpha'}}{\partial \phi_{\alpha}} + 2C_{1212}^{\alpha'}\frac{\partial \epsilon_{12}^{SAS,\alpha'}}{\partial \phi_{\alpha}} \tag{C.8}$$

$$\text{with } \frac{\partial \epsilon_{kl}^{SAS,\alpha'}}{\partial \phi_{\alpha}} = [\phi_{\alpha} I + \sum_{\rho \neq \alpha} M_{klmn}^{\rho'}]^{-1}[-\epsilon_{kl}^{*,\alpha'} - \epsilon_{kl}^{SAS,\alpha'}]$$

$$\text{and } \frac{\partial \epsilon_{kl}^{SAS,\rho'}}{\partial \phi_{\alpha}} = M_{klmn}^{\rho'}\frac{\partial \epsilon_{kl}^{SAS,\alpha'}}{\partial \phi_{\alpha}} \tag{C.9}$$

where $M_{klmn}^{\rho'} = [C_{ijkl}^{\rho'}]^{-1}C_{ijmn}^{\alpha'}$.

Appendix D. Model validation for two-phase systems

We consider a 3D laminate structure of size 2×64×2 grid points made of alternating domains of α and β (Figure D.9a) with equal stiffnesses subjected to a tensile strain along x direction. This is similar to the structure considered by Cottura *et al.* [24] for which

they have provided analytical solution of the strain state. There is assumed to be no misfit between the two phases, so the eigenstrain is zero. Plastic deformation happens only in the β phase and α is an elastic phase. No hardening is considered in the β phase. The non-dimensional parameters used in this simulation are listed in Table D.4. They do not correspond to physical values and have been scaled down in order to speed up the simulations. The stiffnesses in the two phases are assumed to be isotropic with $C_{1111} = 197000$, $C_{1122} = 144000$, and $C_{1212} = 90000$. The interpolation function for two-phase systems is taken as $\phi_\alpha = \mathrm{p}(\phi) = \phi^3(6\phi^2 - 15\phi + 10)$ and $\phi_\beta = 1$ - $\mathrm{p}(\phi)$.

Appendix D.1. Frozen structure

First, we consider a frozen microstructure, i.e., the phase-field variables do not become diffuse at the interface. The kinetic parameters L and M are taken to be zero in order to ensure this. Tensile strain is applied in the x direction (see Figure D.9a) starting from 1.775×10^{-3} (this generates von Mises stress less than yield stress) until 1.82×10^{-3} with an increment of 1×10^{-10} in each time step.

When the stress exceeds the yield stress, the plastic strain evolution begins in the β phase as expected. At a final applied strain of 1.82×10^{-3}, the cumulative plastic strain profile is given in Figure D.9b. The plastic strain evolves such that the von Mises stress remains at the value of the yield stress as expected, since we assume that there is no hardening in the β phase. The plastic strain components are shown in Figure D.9c. As expected from the analytical solution [24], $\epsilon_{11}^{pl,\beta} = p^\beta$ $(= 1.4453 \times 10^{-4})$, and $\epsilon_{22}^{pl,\beta} = \epsilon_{33}^{pl,\beta} = -p^\beta/2$ $(= -7.2267 \times 10^{-5})$.

Appendix D.2. Introducing diffuse interface

After stopping the simulation when the applied tensile strain reaches 1.82×10^{-3}, we introduce the diffuse interface in order to study the evolution of composition and check the interpolation of the viscoplastic energy across the diffuse interface. L and M now take values as listed in Table D.4. The simulations are run until equilibrium is reached.

Figure D.10a shows the elastic strain profiles that are obtained. ϵ_{22}^{el} is non-zero only in the β phase due to the plastic strain contribution, since the applied and heterogeneous strains are uniform and zero throughout the system as expected [24].

Table D.4: Input parameters (non-dimensional) used for the simulations

Parameter	**3D-AppliedStrain**
System size	2×64×2
Time step	10
Grid size	1
M	10^{-7}
L	10^{-5}
A^{α}	10^{3}
A^{β}	10^{3}
$c_{\alpha,0}$	0.2
$c_{\beta,0}$	0.8
W	1.1002
κ	4.0901
R^{α}	10^{5}
R^{β}	86
K^{α}	150
K^{β}	150
n^{α}	5
n^{β}	5
Applied strain	0.001775 to 0.00182
Applied stress	0
Eigenstrain	0

In quantitative phase-field models, the addition of strain energy is not expected to contribute to excess energy at the diffuse interface which is not present in sharp interface descriptions. In order to verify this, we plot the elastic and viscoplastic energy densities as a function of the interpolation function $p(\phi)$ (Figures D.10b and D.10c). The elastic and viscoplastic energy densities both follow a linear interpolation with respect to $p(\phi)$, thus

confirming that there are no excess interfacial energy contributions from the strain energy formulation (see Chapter [18]).

The compositions also change from their equilibrium values (0.2 and 0.8) with no strains. The new compositions in the two phases are 0.20002 and 0.80002 respectively. If there is no plastic deformation, the deviation in composition may be calculated using [89]. However, the elastic stresses are now relaxed by the viscoplastic deformation. To the best of our knowledge, there are no analytical relations to directly calculate the composition change when both elastic and plastic strains are present in the system. In our previous studies (Chapters [18] and [30]), we have shown that the composition deviation is captured well by the phase-field model considering elastic energy. Therefore, the phase-field model may also be used to determine the composition deviation due to elastic and plastic deformation in cases where analytical solutions are not available as long as the relevant strain energies are considered in a quantitative phase-field framework.

Appendix E. Model validation for multi-phase systems

As mentioned in Section 2, in quantitative phase-field models, the presence of the diffuse interface does not give rise to excess energy. Since this is the first time we introduce our elastic energy scheme for multi-phase systems, we verify that this is indeed the case. A similar validation for two-phase systems may be found in [35]. To demonstrate this, the elastic energy density at 100000 s is plotted as a function of ϕ_{Fcc} and ϕ_{Cu_3Sn} at the Fcc-Cu/Cu_3Sn interface for case 'NoApp_LowEig' in Figure E.11a. The elastic energy density interpolates linearly with ϕ_{Fcc} and ϕ_{Cu_3Sn}. Therefore, there is no excess energy generated at the interface due to the elastic energy formulation [18]. Similar plots for viscoplastic energy density at 100000s at the interface between Cu_6Sn_5 and Bct-Sn phases for case 'NoApp_EqEig' in Figure E.11b show that there is no excess energy generated due to the viscoplastic energy formulation also.

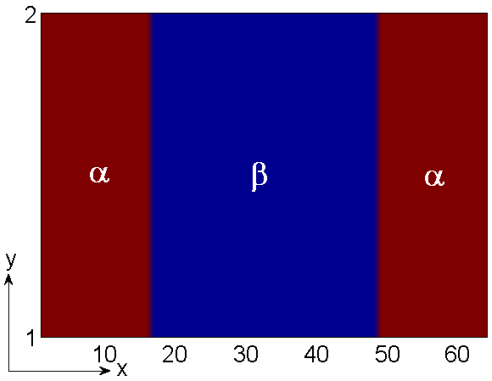

(a)

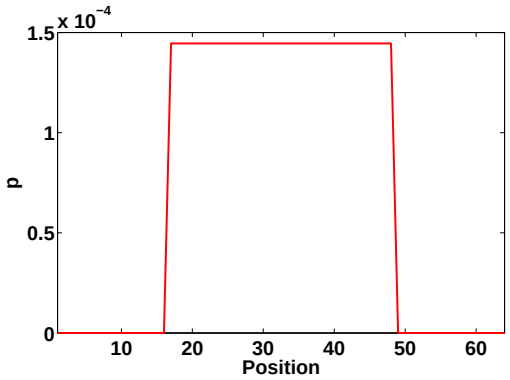

(b)

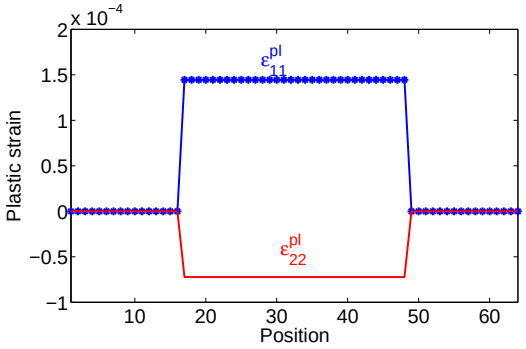

(c)

Figure D.9: Simulation results (with non-dimensional parameters) for a laminate structure with applied strain: (a) Initial structure (figure not to scale) (b) Cumulative plastic strain profile for β phase (c) Plastic strain profiles of components ϵ_{11}^{pl} and ϵ_{22}^{pl}.

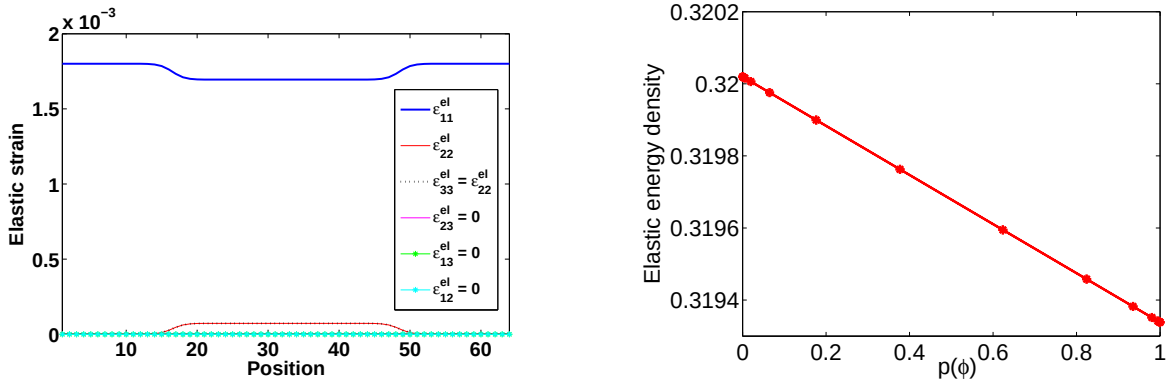

(a)

(b)

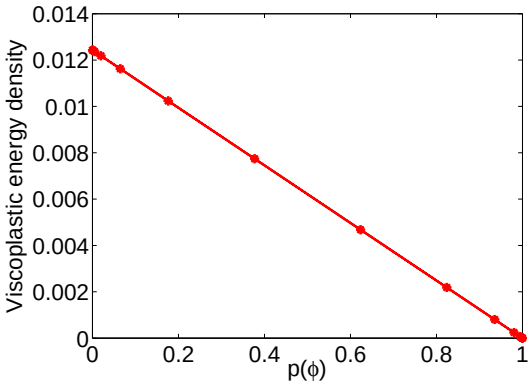

(c)

Figure D.10: Simulation results (with non-dimensional parameters) for a laminate structure with applied strain: (a) Elastic strain profiles after introducing a diffuse interface (b) Elastic energy interpolation with respect to $p(\phi)$ (c) Viscoplastic energy interpolation with respect to $p(\phi)$

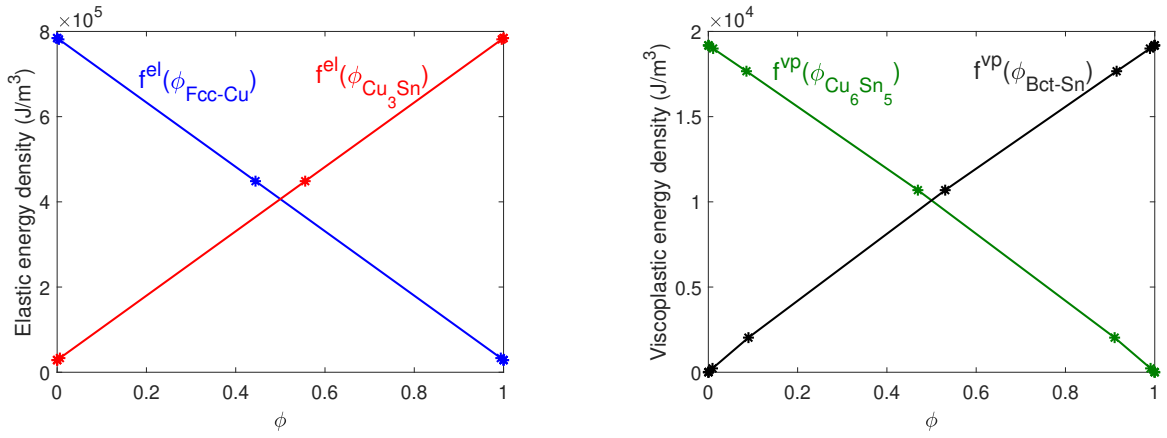

Figure E.11: (a) Linear interpolation of elastic energy density with respect to ϕ_{Fcc-Cu} and ϕ_{Cu_3Sn} across the interface between Fcc and Cu_3Sn for case 'NoApp_LowEig' at 100000 s shows that there is no excess energy at the interface due to the elastic energy formulation, (b) Similar plots for the viscoplastic energy density at the interface between Cu_6Sn_5 and Bct-Sn for case 'NoApp_EqEig' at 100000 s shows that there is no excess energy due to the viscoplastic energy forumation.